J. Fluid Mech. (2022), *vol*. 940, A20, doi:10.1017/jfm.2022.228

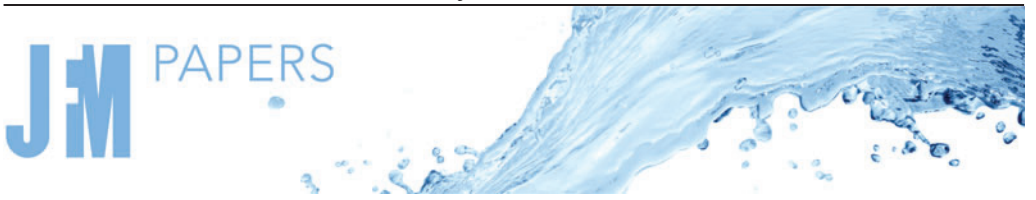

Effects of spanwise-periodic surface heating on supersonic boundary-layer instability

Kaixin Zhu[1] **and Xuesong Wu**[1,2,†]

[1]Department of Mechanics, Tianjin University, Tianjin 300072, PR China

[2]Department of Mathematics, Imperial College London, 180, Queen's Gate, London SW7 2AZ, UK

(Received 6 September 2021; revised 16 January 2022; accepted 9 March 2022)

The effects of streamwise-elongated, spanwise-periodic surface heating on a supersonic boundary-layer instability are investigated under the assumption of high Reynolds number. Our focus is on the lower-branch viscous instability and so the spanwise spacing of the elements is chosen to be of $O(Re^{-3/8}L)$, the wavelength of the latter, where Re is the Reynolds number based on L, the distance from the leading edge to the centre of the elements. The streamwise length is assumed to be much longer in order to simplify the mathematical description. Starting with classical triple-deck theory, the equations governing the heating-induced streaky flow are derived by appropriate rescaling. When Chapman's viscosity law is adopted, a similarity solution is found. The stability of the streaky flow, which is of a bi-global nature, is shown to be governed by a novel triple-deck structure characterised by fully compressible dynamics in the lower deck. Through asymptotic analysis, the bi-global stability is reduced to a one-dimensional eigenvalue problem, which involves only the spanwise-dependent wall temperature and wall shear. The instability modes may be viewed as a continuation of oncoming first Mack modes, but might also be considered as a new kind since they exhibit two distinctive features: strong temperature perturbation near the wall and spontaneous radiation of an acoustic wave to the far field, neither of which is shared by first Mack modes. Numerical calculations, performed for two simple patterns of spanwise-periodic heating elements, demonstrate their stabilising/destabiling effects on modes with different frequencies and spanwise wavelengths.

Key words: boundary layer stability, supersonic flow, transition to turbulence

1. Introduction

Surface heating/cooling, as a flow control technique, has received much attention owing to its proved and perceived applications. In a supersonic boundary layer, spatially

† Email address for correspondence: x.wu@ic.ac.uk

uniform heating/cooling was found to destabilise/stabilise the first Mack modes but stabilise/destabilise the second modes (Mack 1975; Lysenko & Maslov 1984). Local heating/cooling has been considered to be more efficient if it is imposed at appropriate positions. The possibility of stabilising flow via a local heating strip centred near, or at upstream of, the lower branch of the neutral curve has been demonstrated experimentally by Dovgal, Levchenko & Timopeev (1990) and numerically by Kral *et al.* (1994). The findings were broadly confirmed by the linear stability analysis of the heating-modified base flow (Masad & Nayfeh 1992; Masad 1995). Hypersonic boundary-layer stability on a cone with localised surface heating/cooling has been studied by Fedorov *et al.* (2015).

While steady heating/cooling influences transition by modifying the base-flow profile, time-periodic and streamwise localised surface heating/cooling has been employed to excite instability modes in a controlled manner (Corke & Mangano 1989). In particular, it may generate a mode with an appropriate amplitude and phase so as to cancel an oncoming wave whereby delaying transition. For incompressible boundary layers, this was demonstrated by the experiments of Liepmann, Brown & Nosenchuck (1982) and Liepmann & Nosenchuck (1982). Direct numerical simulations of transition control through excitation and cancellation of instability modes by time-periodic heating were performed by Kral & Fasel (1991). A theoretical description was developed recently by Brennan, Gajjar & Hewitt (2021) based on triple-deck formalism.

Classical triple-deck theory (Neiland 1969; Stewartson & Williams 1969) has been extended to the boundary layer subject to local temperature disturbances. In the case of a two-dimensional $O(1)$ temperature variation occurring on the triple-deck scale, the problem was formulated by Méndez, Treviño & Liñán (1992) for a wall temperature jump, and the boundary layer was found to separate when the jump exceeds a critical value. Treviño & Liñán (1996) analysed how surface temperature disturbances of moderate intensity modify the growth rate of the instability using a perturbation approach. This perspective of local stability is however inappropriate because the length scales of the instability and the heating-induced mean-flow alteration are comparable. Instead the impact on instability should be accounted for by a local scattering approach (Wu & Hogg 2006; Wu & Dong 2016). Lipatov (2006) developed asymptotic theories for three-dimensional surface heating elements with different length scales. The effect of heating is shown to be equivalent to that of a local roughness element. For heating on the triple-deck scale, Koroteev & Lipatov (2009, 2012) obtained linear solutions analytically and nonlinear solutions numerically. The asymptotic theory has also been extended by Aljohani & Gajjar (2017*a*,*b*, 2018) to investigate the impact of two- and three-dimensional heated roughness elements on subsonic and transonic boundary layers.

The present paper is concerned with spanwise-periodic streamwise-elongated surface heating and its effects on supersonic boundary-layer instability. Such a problem has not been investigated before although its counterpart for roughness arrays of this form in an incompressible boundary layer has been studied by Kátai & Wu (2020), where a stabilising effect was identified for weakly three-dimensional lower-frequency instability modes. As will be shown, such a form of surface heating in supersonic boundary layers causes significantly different instability characteristics.

The rest of the paper is organized as follows. In § 2 the problem is formulated. We first derive the simplified mathematical system governing the three-dimensional streaky flow induced by surface heating. Under the assumption of Chapman's viscosity law, the similarity solution is then obtained and presented. In § 3 the stability of the streaky flow is considered, and we show that the instability is governed by a new triple-deck structure with the dynamics in the lower deck being fully compressible. The bi-global eigenvalue

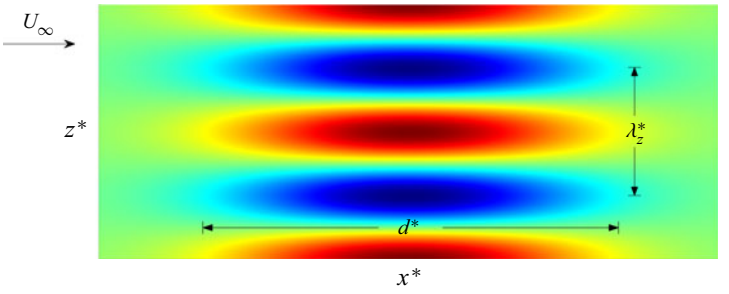

Figure 1. Schematics of a streaky flow induced by an array of spanwise-periodic surface heating elements. The contours show the surface temperature distribution, where x^* and z^* represent the streamwise and spanwise coordinates, λ_z^* and d^* denote the spanwise wavelength and streamwise extent of the heating elements, and U_∞ the free-stream velocity.

problem is reduced to a one-dimensional one in the spanwise direction, and the instability is shown to be controlled by the spanwise-dependent wall shear and temperature. The reduced eigenvalue problem is solved, and numerical results are presented in § 4 to highlight the main instability characteristics. A summary and conclusions are given in § 5.

2. Problem formulation

2.1. *Heating elements on the triple-deck scale*

We consider a supersonic boundary layer flow past a semi-infinite flat plate, on which an array of streamwise-elongated and spanwise-periodic heating elements is deployed, as is shown figure 1. The elements are centred at a distance L from the leading edge. First we introduce the dimensionless variables

$$\left.\begin{gathered}(x, y, z) = (x^*, y^*, z^*)/L, \quad (u, v, w) = (u^*, v^*, w^*)/U_\infty, \\ p = (p^* - p_\infty)/(\rho_\infty U_\infty^2), \quad \rho = \rho^*/\rho_\infty, \quad T = T^*/T_\infty, \quad \mu = \mu^*/\mu_\infty,\end{gathered}\right\} \tag{2.1}$$

where (x, y, z) are Cartesian coordinates with the origin located at the centre of the elements, (u, v, w) are the corresponding velocities, p, ρ, T and μ denote the pressure, density, temperature and dynamic viscosity coefficient, respectively. We use an asterisk to indicate dimensional quantities and ∞ the quantities in the free stream. The Reynolds number Re and Mach number M_∞ are defined as

$$Re = \rho_\infty U_\infty L/\mu_\infty, \quad M_\infty = U_\infty/a_\infty, \tag{2.2a,b}$$

with a_∞ being the speed of sound in the free stream. It is assumed that $Re \gg 1$ in order to present the asymptotic descriptions of the heating-induced streaky flow and its viscous instability. The focus will be on $1 < M_\infty < 4.5$, in which the first mode plays a dominant role in transition.

We begin with a standard triple-deck structure whose streamwise and spanwise length scales are of $O(Re^{-3/8}L)$. The asymptotic description of the flow induced by such a form of heating was presented by Lipatov (2006). It is convenient to use the rescaled coordinates

$$\{X, Z\} = \epsilon^{-3}\{x, z\}, \quad \{y_1, y_2, y_3\} = \{\epsilon^{-3}y, \epsilon^{-4}y, \epsilon^{-5}y\}, \quad \epsilon = Re^{-1/8}, \tag{2.3a,b}$$

where y_1, y_2 and y_3 are the local coordinates in the upper, main and lower decks, respectively. We assume that the wall temperature is varied by $O(1)$ through heating.

The induced velocity field near the surface is of $O(\epsilon)$. Specifically, in the lower deck where $y_3 = O(1)$, the dependent variables have the expansions (Lipatov 2006)

$$\{u, w\} = \epsilon\{u_3, w_3\} + O(\epsilon^2), \quad v = \epsilon^3 v_3 + O(\epsilon^4), \tag{2.4a,b}$$

$$p = \epsilon^2 p_3 + O(\epsilon^3), \quad \{\rho, T, \mu\} = \{\rho_3, T_3, \mu_3\} + O(\epsilon). \tag{2.5a,b}$$

Substitution into the Navier–Stokes (NS) equations leads to the governing equations of the lower deck,

$$\frac{\partial(\rho_3 u_3)}{\partial X} + \frac{\partial(\rho_3 v_3)}{\partial y_3} + \frac{\partial(\rho_3 w_3)}{\partial Z} = 0, \tag{2.6}$$

$$\rho_3\left(u_3\frac{\partial u_3}{\partial X} + v_3\frac{\partial u_3}{\partial y_3} + w_3\frac{\partial u_3}{\partial Z}\right) = -\frac{\partial p_3}{\partial X} + \frac{\partial}{\partial y_3}\left(\mu_3\frac{\partial u_3}{\partial y_3}\right), \tag{2.7}$$

$$\rho_3\left(u_3\frac{\partial w_3}{\partial X} + v_3\frac{\partial w_3}{\partial y_3} + w_3\frac{\partial w_3}{\partial Z}\right) = -\frac{\partial p_3}{\partial Z} + \frac{\partial}{\partial y_3}\left(\mu_3\frac{\partial w_3}{\partial y_3}\right), \tag{2.8}$$

$$\rho_3\left(u_3\frac{\partial T_3}{\partial X} + v_3\frac{\partial T_3}{\partial y_3} + w_3\frac{\partial T_3}{\partial Z}\right) = \frac{\partial}{\partial y_3}\left(\mu_3\frac{\partial T_3}{\partial y_3}\right), \tag{2.9}$$

with the y-momentum equation giving $\partial p_3/\partial y_3 = 0$ and the state equation $\rho_3 T_3 = 1$, where we assume that the specific heat capacities are constant and the Prandtl number Pr is unity. The matching and boundary conditions of the above system are

$$u_3 \to \lambda_B y_3, \quad w_3 \to 0, \quad T_3 \to T_B(0) \quad \text{as } X \to -\infty; \tag{2.10a,b}$$

$$u_3 = v_3 = w_3 = 0, \ T_3 = T_w(X, Z) \quad \text{at } y_3 = 0; \tag{2.11a,b}$$

$$u_3 \to \lambda_B(A(X, Z) + y_3), \quad w_3 \to \frac{D(X, Z)}{\lambda_B y_3 \rho_B(0)}, \quad T_3 \to T_B(0) \quad \text{as } y_3 \to \infty, \tag{2.12a–c}$$

among which (2.10a,b) represents the matching with the unperturbed state upstream (and serves as the leading-order initial condition when elongated heating arrays are considered later). In (2.10a,b)–(2.12a–c), $\lambda_B = 0.3321 T_B^{-1}(0)$ is the wall shear of the compressible Blasius flow, $T_B(y_2)$ and $\rho_B(y_2)$ are the corresponding temperature and density profiles, of which $T_B(y_2)$ is related to the velocity profile $u_B(y_2)$ via $T_B = 1 + (\gamma - 1)M_\infty^2(1 - u_B^2)/2$ under the assumption that the unperturbed wall temperature takes the adiabatic value with γ denoting the ratio of the specific heat capacities. These unperturbed flow quantities are evaluated at $x = 0$, the 'centre' of the heating elements (and at $y_2 = 0$ if the argument is set to zero). The function $T_w(X, Z)$ represents the wall temperature imposed by the heating elements. The unknown functions $D(X, Z)$ and $A(X, Z)$ are introduced with D satisfying $\partial D/\partial X = -\partial P/\partial Z$ and A being the displacement function.

In the main deck, where $y_2 = O(1)$, we express the dependent variables as

$$u = u_B + \epsilon u_2 + O(\epsilon^2), \quad \{v, w\} = \epsilon^2\{v_2, w_2\} + O(\epsilon^3), \tag{2.13a,b}$$

$$p = \epsilon^2 p_2 + O(\epsilon^3), \quad \{\rho, T\} = \{\rho_B, T_B\} + \epsilon\{\rho_2, T_2\} + O(\epsilon^2). \tag{2.14a,b}$$

Substitution of the above expansions into the NS equations leads to the equations governing the main-deck disturbance, and their leading-order solution can be found as

$$u_2 = A(X, Z)\frac{\mathrm{d}u_B}{\mathrm{d}y_2}, \quad v_2 = -\frac{\partial A(X, Z)}{\partial X}u_B, \quad w_2 = \frac{D(X, Z)}{u_B\rho_B}, \tag{2.15a–c}$$

$$p_2 = P(X, Z), \quad T_2 = A(X, Z)\frac{\mathrm{d}T_B}{\mathrm{d}y_2}, \tag{2.16a,b}$$

where the function $P(X, Z)$ is introduced to denote the pressure in the lower deck, i.e. $p_3 = P(X, Z)$, which is independent of the transverse coordinate. The main deck plays a passive role of conveying the displacement effect produced in the lower deck to the upper deck.

In the upper deck, where $y_1 = O(1)$, the displacement-induced pressure can be expanded as $p = \epsilon^2 p_1 + O(\epsilon^3)$, where p_1 is governed by

$$\left(M_\infty^2 - 1\right) \frac{\partial^2 p_1}{\partial X^2} - \frac{\partial^2 p_1}{\partial y_1^2} - \frac{\partial^2 p_1}{\partial Z^2} = 0, \tag{2.17}$$

and subjected to the matching and boundary conditions

$$\left.\frac{\partial p_1}{\partial y_1}\right|_{y_1=0} = \frac{\partial^2 A}{\partial X^2}, \quad p_1|_{y_1=0} = P(X, Z), \quad p_1|_{y_1\to\infty} \to 0. \tag{2.18a–c}$$

The solution to the boundary-value problem (2.17)–(2.18*a–c*) leads to the so-called pressure-displacement relation.

2.2. *Streaky flow induced by streamwise-elongated heating elements*

Surface heating with both streamwise and spanwise lengths on the triple-deck scale is of interest, but its impact on stability must be accounted for by an extension of the local scattering approach (Wu & Dong 2016), which is computationally expensive. We now consider elongated heating elements whose spanwise length scale remains unchanged but the streamwise length scale d^* is stretched to $O(\epsilon^3 \epsilon_x^{-1})L$, where $\epsilon_x \ll 1$ is the aspect ratio, i.e. the ratio of the spanwise spacing and streamwise extent of the heating elements. This is a departing point from the previous work (Koroteev & Lipatov 2009, 2012). The order of magnitude of ρ_3, T_3 and μ_3 remains $O(1)$. A simplified structure arises after appropriate balances. We first introduce the rescaled independent and dependent variables,

$$\{\bar{X}, \bar{y}_3, \bar{A}\} = \{\epsilon_x X, \epsilon_y y_3, \epsilon_a A\}, \tag{2.19}$$

$$\{\bar{u}_3, \bar{v}_3, \bar{w}_3, \bar{p}_3\} = \{\epsilon_u u_3, \epsilon_v v_3, \epsilon_w w_3, \epsilon_p p_3\}, \tag{2.20}$$

where rescaling factors ϵ_y, ϵ_u, ϵ_v, ϵ_w, ϵ_p and ϵ_a are to be found. In the lower deck, all three terms in the continuity equation (2.6) balance, and the inertial and viscous terms balance in momentum equations (2.7) and (2.8). The terms in the matching condition (2.12*a*) balance. Meanwhile, the matching condition (2.18*a*) holds. These balances lead to six relations,

$$\frac{\epsilon_x}{\epsilon_u} = \frac{\epsilon_y}{\epsilon_v} = \frac{1}{\epsilon_w}, \quad \frac{\epsilon_x}{\epsilon_u} = \epsilon_y^2, \quad \epsilon_u = \epsilon_y = \epsilon_a, \quad \frac{1}{\epsilon_p} = \frac{\epsilon_x^2}{\epsilon_a}, \tag{2.21a–d}$$

from which the six rescaling factors are expressed in terms of ϵ_x,

$$\{\epsilon_y, \epsilon_u, \epsilon_v, \epsilon_w, \epsilon_p, \epsilon_a\} = \{\epsilon_x^{1/3}, \epsilon_x^{1/3}, \epsilon_x^{-1/3}, \epsilon_x^{-2/3}, \epsilon_x^{-5/3}, \epsilon_x^{1/3}\}. \tag{2.22}$$

Substitution of (2.19)–(2.20) with (2.22) into (2.6)–(2.9) leads to the equations governing the lower-deck flow,

$$\frac{\partial\left(\rho_3\bar{u}_3\right)}{\partial\bar{X}}+\frac{\partial\left(\rho_3\bar{v}_3\right)}{\partial\bar{y}_3}+\frac{\partial\left(\rho_3\bar{w}_3\right)}{\partial Z}=0, \tag{2.23}$$

$$\rho_3\left(\bar{u}_3\frac{\partial\bar{u}_3}{\partial\bar{X}}+\bar{v}_3\frac{\partial\bar{u}_3}{\partial\bar{y}_3}+\bar{w}_3\frac{\partial\bar{u}_3}{\partial Z}\right)=\frac{\partial}{\partial\bar{y}_3}\left(\mu_3\frac{\partial\bar{u}_3}{\partial\bar{y}_3}\right), \tag{2.24}$$

$$\rho_3\left(\bar{u}_3\frac{\partial\bar{w}_3}{\partial\bar{X}}+\bar{v}_3\frac{\partial\bar{w}_3}{\partial\bar{y}_3}+\bar{w}_3\frac{\partial\bar{w}_3}{\partial Z}\right)=\frac{\partial}{\partial\bar{y}_3}\left(\mu_3\frac{\partial\bar{w}_3}{\partial\bar{y}_3}\right), \tag{2.25}$$

$$\rho_3\left(\bar{u}_3\frac{\partial T_3}{\partial\bar{X}}+\bar{v}_3\frac{\partial T_3}{\partial\bar{y}_3}+\bar{w}_3\frac{\partial T_3}{\partial Z}\right)=\frac{\partial}{\partial\bar{y}_3}\left(\mu_3\frac{\partial T_3}{\partial\bar{y}_3}\right), \tag{2.26}$$

$$\frac{\partial\bar{p}_3}{\partial\bar{y}_3}=0,\quad \rho_3T_3=1, \tag{2.27a,b}$$

and the boundary and matching conditions (2.10*a*,*b*)–(2.12*a*–*c*) take on the rescaled form

$$\bar{u}_3\to\lambda_B\bar{y}_3,\quad \bar{w}_3\to 0,\quad T_3\to T_B(0)\quad \text{as } \bar{X}\to-\infty; \tag{2.28a–c}$$

$$\bar{u}_3=\bar{v}_3=\bar{w}_3=0,\quad T_3=T_w(\bar{X},Z)\quad \text{on } \bar{y}_3=0; \tag{2.29a,b}$$

$$\bar{u}_3\to\lambda_B(\bar{y}_3+\bar{A}),\quad \bar{w}_3\to 0,\quad T_3\to T_B(0)\quad \text{as } \bar{y}_3\to\infty. \tag{2.30a–c}$$

In the upper deck, the pressure is rescaled as $\bar{p}_1=\epsilon_x^{-5/3}p_1$. Since the streamwise derivative of the pressure is relatively small, the governing equation (2.17) reduces to

$$\frac{\partial^2\bar{p}_1}{\partial y_1^2}+\frac{\partial^2\bar{p}_1}{\partial Z^2}=0, \tag{2.31}$$

with the matching conditions (2.18*a*–*c*) remaining unchanged.

2.3. *Solutions of the lower deck*

We first consider the boundary-value problem for $\bar{w}_3$ consisting of the z-momentum equation (2.25) together with the vanishing initial and boundary conditions of $\bar{w}_3$ in (2.28*a*–*c*)–(2.30*a*–*c*). Based on this system, an analogy (or equivalence) may be drawn between $\bar{w}_3$ and a passive scalar that is advected and undergoes diffusion. The homogeneous upstream and boundary conditions imply that no scalar is introduced to the flow field, and it follows that $\bar{w}_3\equiv 0$. Alternatively and more mathematically, according to the weak maximum principle of parabolic partial differential equations (Renardy & Rogers 2006), the spanwise velocity $\bar{w}_3$ is identically zero. Therefore, the elongated-element induced streaky flow can, despite its three-dimensional nature, be calculated in a quasi-two-dimensional manner. This is a simple but useful result as it allows for simplification of the computations. However, a numerical approach still has to be taken for a general viscosity law.

When Chapman's viscosity law is adopted, for which $\mu_3=CT_3$ with $C=1$ for the non-dimensionalisation adopted, and after employing the Dorodnitsyn–Howarth transformation and the associated substitution of the transverse velocity (cf. Aljohani &

Gajjar 2017*b*),

$$\bar{Y}_3(\bar{X},\bar{y}_3,Z)=\int_0^{\bar{y}_3}\rho_3(\bar{X},y,Z)\,\mathrm{d}y,\quad \rho_3\bar{v}_3=\bar{V}_3(\bar{X},\bar{Y}_3,Z)-\bar{u}_3\left.\frac{\partial\bar{Y}_3}{\partial\bar{X}}\right|_{\bar{y}_3},\qquad (2.32a,b)$$

the fully nonlinear equations (2.23)–(2.26) simplify to

$$\frac{\partial\bar{u}_3}{\partial\bar{X}}+\frac{\partial\bar{V}_3}{\partial\bar{Y}_3}=0,\quad \bar{u}_3\frac{\partial\bar{u}_3}{\partial\bar{X}}+\bar{V}_3\frac{\partial\bar{u}_3}{\partial\bar{Y}_3}=\frac{\partial^2\bar{u}_3}{\partial\bar{Y}_3^2},\quad \bar{u}_3\frac{\partial T_3}{\partial\bar{X}}+\bar{V}_3\frac{\partial T_3}{\partial\bar{Y}_3}=\frac{\partial^2 T_3}{\partial\bar{Y}_3^2},\qquad (2.33a\text{–}c)$$

which are the same as in the incompressible case. A seemingly trivial solution to (2.33*a*,*b*) satisfying both the matching and boundary conditions (2.28*a*–*c*)–(2.30*a*–*c*) is found as

$$\bar{u}_3=\frac{\lambda_B}{\rho_B(0)}\bar{Y}_3,\quad \bar{V}_3=0,\quad \bar{A}=\frac{1}{\rho_B(0)}\int_0^\infty[\rho_3-\rho_B(0)]\,\mathrm{d}y.\qquad (2.34a\text{–}c)$$

Therefore, the temperature equation (2.33*c*) simplifies to a linear diffusion equation and can be solved by a marching method first. With the temperature field known, the velocity field can be obtained using (2.34*a*–*c*). Indeed (2.34*a*–*c*) is the appropriate solution with the similarity variable $\bar{Y}_3$ containing both the streamwise and wall-normal coordinates through (2.32*a*). It is rather remarkable that the solution to the fully nonlinear equations (2.23)–(2.26) for the induced three-dimensional flow can be constructed in such a simple procedure; this observation has not been made before to the best of our knowledge.

The lower-deck solutions u_3 and T_3, and main-deck solutions u_2 and T_2, are only valid in their respective regions. A composite solution that is valid in both decks can be constructed by using the additive composition (Van Dyke 1975). On noting the scalings in (2.4*a*,*b*)–(2.5*a*,*b*), (2.13*a*,*b*)–(2.14*a*,*b*) and (2.19)–(2.20) with (2.22) the composite solution for the streamwise velocity and the temperature can be expressed as

$$u^c=\underbrace{\epsilon\epsilon_x^{-1/3}\bar{u}_3(\bar{X},\bar{y}_3,Z)}_{\textit{lower-decksolution}}+\underbrace{u_B(y_2)+\epsilon\epsilon_x^{-1/3}\bar{A}(\bar{X},Z)u_B'(y_2)}_{\textit{main-decksolution}}-\underbrace{\epsilon\epsilon_x^{-1/3}\lambda_B(\bar{y}_3+\bar{A}(\bar{X},Z))}_{\textit{common part}},\qquad (2.35)$$

$$T^c=\underbrace{T_3(\bar{X},\bar{y}_3,Z)}_{\textit{lower-deck solution}}+\underbrace{T_B(y_2)}_{\textit{main-decksolution}}-\underbrace{T_B(0)}_{\textit{common part}}.\qquad (2.36)$$

Numerical calculations of u^c and T^c are performed for the three-dimensional flow induced by a surface temperature distribution of the variable separation form,

$$T_w(\bar{X},Z)=T_B(0)+hf(\bar{X})S(Z),\qquad (2.37)$$

where h measures the heating level, $f(\bar{X})$ is taken to be Gaussian distribution and $S(Z)$ has a Fourier series representation,

$$f(\bar{X})=\exp(-(\bar{X}/d)^2),\quad S(Z)=\sum_{n=0}^{+\infty}s_n\cos(n\beta Z),\qquad (2.38a,b)$$

where d is the rescaled length measuring the streamwise extent, and β the spanwise wavenumber, of the heating elements. For simplicity, in our calculations we take $s_1=1$ and $s_n=0$ for all $n\neq 1$, i.e.

$$S(Z)=\cos(\beta Z).\qquad (2.39)$$

Other parameter values are: $M_\infty=3$, $\gamma=1.4$ (in air), $d=0.5$, $\beta=2\pi$ and $h=1$, which corresponds to heating with the maximum surface temperature variation being the same

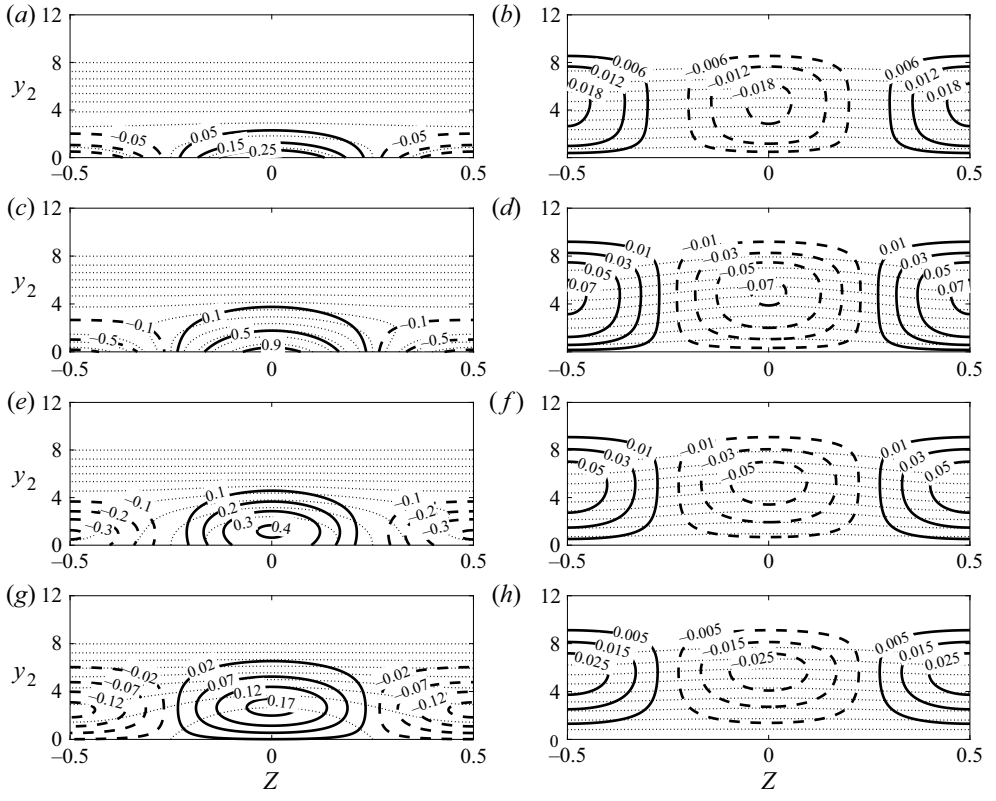

Figure 2. (a,c,e,g) Contours of the composite temperature T^c (dotted lines) and its deviation from the Blasius flow, $T^c - T_B$ (solid and dashed lines); (b,d,f,h) contours of the composite streamwise velocity u^c (dotted lines) and its deviation from the Blasius flow, $u^c - u_B$ (solid and dashed lines). Results are shown for (a,b) $\bar{X} = -0.5$; (c,d) $\bar{X} = 0$; (e,f) $\bar{X} = 0.5$; (g,h) $\bar{X} = 1$. Parameters: $\epsilon = 0.2$, $\epsilon_x = 0.06$.

as the free-stream temperature, or 36 % of the unperturbed adiabatic surface temperature since $T_B(0) = 2.8$. We take $\epsilon = 0.2$ (which corresponds to a typical Reynolds number $Re \approx 5 \times 10^5$) and $\epsilon_x = 0.06$ as in Kátai & Wu (2020), where these values are pertinent to the experiment of Downs & Fransson (2014). Figure 2 shows in the y_2–Z plane the contours of the composite streamwise velocity and temperature, u^c and T^c, and their deviation from the Blasius flow, $u^c - u_B$ and $T^c - T_B$, at four different streamwise locations. The form of streaks can be observed in both the velocity and temperature deviations. High-temperature low-speed streaks arise at the centreline of the heating ($Z = 0$), along with low-temperature high-speed streaks at $Z = \pm 0.5$. While the temperature field T^c exhibits obvious three dimensionality, the velocity u^c as shown in the figure varies weakly in the spanwise direction. This is due to the fact that in the main layer the heating-induced spanwise-varying velocity is much smaller than, and, hence, masked by, the Blasius flow. The former is comparable with the latter only in the region closer to the wall. A zoomed view of this part of the flow is displayed in figure 3, and a significant spanwise variation is observed for $-0.5 \leq \bar{X} \leq 0.5$, and indeed $u^c \approx \epsilon \epsilon_x^{-1/3} \lambda_u(\bar{X}, Z)\bar{y}_3$ as expected, where λ_u represents the rescaled wall shear of the streaky flow.

As the flow depends on both the transverse and spanwise coordinates, the instability is in general of a bi-global type (Theofilis 2011). However, our concern is with the lower-branch viscous instability, which will later be shown to be controlled by the wall shear λ_u and wall

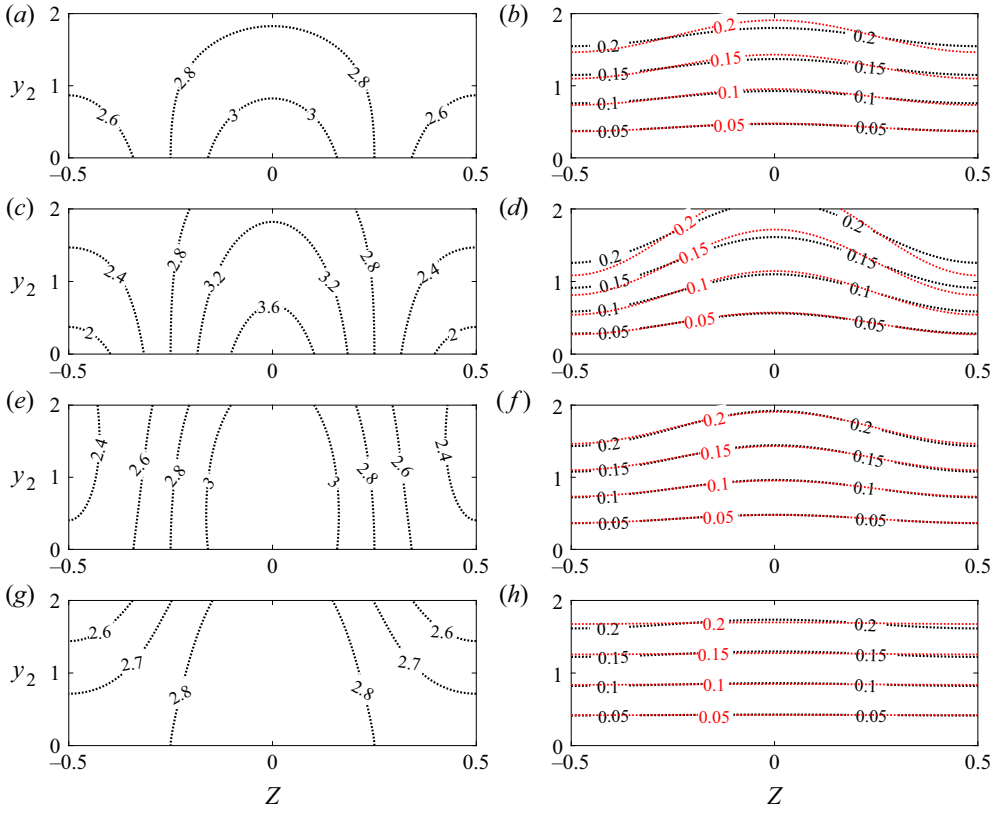

Figure 3. A zoomed near-wall view of the flow shown in figure 2. Results are shown for (*a*,*b*) $\bar{X} = -0.5$; (*c*,*d*) $\bar{X} = 0$; (*e*,*f*) $\bar{X} = 0.5$; (*g*,*h*) $\bar{X} = 1$. Black lines: T^c (*a*,*c*,*e*,*g*) and u^c (*b*,*d*,*f*,*h*); red lines: $\epsilon\epsilon_x^{-1/3}\lambda_u\bar{y}_3$.

temperature T_w only. Interestingly, the wall shear λ_u has the analytical expression

$$\lambda_u(\bar{X}, Z) = \left.\frac{\partial \bar{u}_3}{\partial \bar{y}_3}\right|_{\bar{y}_3=0} = \lambda_B \frac{\rho_3(\bar{X}, 0, Z)}{\rho_B(0)} = \lambda_B \frac{T_B(0)}{T_w(\bar{X}, Z)}, \tag{2.40}$$

which can be calculated without solving for the flow field in the boundary layer. The constant λ_B will be set to unity on the understanding that the dependence on it is accounted for by the rescaling as in Smith (1989).

3. Linear stability analysis of the streaky boundary layer

Lower-branch Tollmien–Schlichting (T-S) modes of a subsonic boundary layer are well known to be governed by the triple-deck structure (Lin 1946; Smith 1979*b*). As continuation of oblique T-S modes into the supersonic regime, first Mack modes are also shown to have the triple-deck scales with the wavelength being of $O(\epsilon^3)$ and the frequency $O(\epsilon^{-2})$ (Smith 1989). These scales carry over to the viscosity instability of the heating-induced streaky flow. Therefore, we introduce the rescaled time variable, $\hat{t} = \epsilon^{-2}t$, for instability analysis. The instability remains being governed by the same triple-deck structure but the lower-deck dynamics differs significantly from that in the classical settings (Smith 1979*b*, 1989) and in incompressible streaky flows (Kátai & Wu 2020). By taking advantage of the triple-deck structure, the dependence of the mode on the

vertical coordinate can be treated analytically, thereby reducing the bi-global instability to a one-dimensional eigenvalue problem in the spanwise direction.

3.1. *Main deck*

In the main deck, the perturbed flow field can be expanded as

$$\{u, v, w\} = \{u_{2b}, \epsilon^2\epsilon_x^{2/3}v_{2b}, \epsilon^2\epsilon_x^{2/3}w_{2b}\} + \epsilon\epsilon_d\{\hat{u}_2, \epsilon\hat{v}_2, \epsilon\hat{w}_2\}E, \tag{3.1}$$

$$\{p, \rho, T\} = \{\epsilon^2\epsilon_x^{5/3}p_{2b}, \rho_{2b}, T_{2b}\} + \epsilon\epsilon_d\{\epsilon\hat{p}_2, \hat{\rho}_2, \hat{T}_2\}E, \tag{3.2}$$

where the quantities with a subscript b signify those of the base flow, the second terms represent a normal-mode disturbance, in which $\epsilon_d \ll 1$ denotes its amplitude and $E = \exp[\mathrm{i}(\alpha X - \omega\hat{t})]$ with α and ω being of $O(1)$. For spatial stability, ω is real denoting the frequency and $\alpha = \alpha_r + \mathrm{i}\alpha_i$ is complex with α_r being the wavenumber and $(-\alpha_i)$ the growth rate. The relative orders of magnitude of the velocity, pressure and density (temperature) of the disturbance, as indicated by (3.1)–(3.2), are the same as those for the viscous first mode (Smith 1989). This is because the present instability retains the spatial and temporal scales of the latter, while the heating-induced mean-flow distortion amounts to a small correction to the Blasius flow. Substituting (3.1)–(3.2) into the NS equations and solving the resultant equations, we obtain the leading-order solution,

$$\hat{u}_2 = A_1\frac{\partial u_{2b}}{\partial y_2}, \quad \hat{v}_2 = -\mathrm{i}\alpha A_1 u_{2b}, \quad \hat{w}_2 = -\frac{1}{\mathrm{i}\alpha\rho_{2b}u_{2b}}\frac{\partial\hat{p}_2}{\partial Z}, \tag{3.3a–c}$$

$$\hat{p}_2 = \hat{p}_2(Z), \quad \hat{T}_2 = A_1\frac{\partial T_{2b}}{\partial y_2}, \tag{3.4a,b}$$

where $A_1(Z)$ is introduced as the displacement function.

3.2. *Lower deck*

In the lower deck, the flow field, consisting of the streaky boundary layer flow and the modal disturbance, expands as

$$\{u, v, w\} = \epsilon\{\epsilon_x^{-1/3}u_{3b}, \epsilon^2\epsilon_x^{1/3}v_{3b}, \epsilon_x^{2/3}w_{3b}\} + \epsilon\epsilon_d\{\hat{u}_3, \epsilon^2\hat{v}_3, \hat{w}_3\}E, \tag{3.5}$$

$$\{p, \rho, T, \mu\} = \{\epsilon^2\epsilon_x^{5/3}p_{3b}, \rho_{3b}, T_{3b}, \mu_{3b}\} + \epsilon_d\{\epsilon^2\hat{p}_3, \hat{\rho}_3, \hat{T}_3, \hat{\mu}_3\}E. \tag{3.6}$$

Since the lower deck for the streaky base flow is much thicker than that for instability modes, we approximate the base-flow quantities by their Taylor expansions about the wall,

$$\{u_{3b}, v_{3b}, w_{3b}\} \approx \epsilon_x^{1/3}\{\lambda_u, \epsilon_x^{1/3}\lambda_v y_3, \lambda_w\}y_3, \quad \{T_{3b}, \rho_{3b}, \mu_{3b}\} \approx \{T_w, \rho_w, \mu_w\}, \tag{3.7a,b}$$

where λ_u is given by (2.40), $\lambda_w = \partial w_{3b}/\partial\bar{y}_3|_{\bar{y}_3=0}$, $\lambda_v = -\frac{1}{2}(\lambda_{u,\bar{X}} + \lambda_{w,Z})$, $T_w = T_w(\bar{X}, Z)$, $\rho_w = 1/T_w$ and $\mu_w = \mu(T_w)$.

Attention should be paid to the asymptotic scalings of the modal disturbance in (3.5)–(3.7*a*,*b*). Its velocity components and pressure have the same scalings as for the viscous first mode (Smith 1989) as a result of the shared characteristic frequency and wavelength. However, due to the presence of the $O(1)$ heating-induced spanwise varying temperature T_{3b}, the spanwise advection induces a temperature disturbance that is greater than the velocity fluctuation by a factor of ϵ^{-1}. This is deduced by considering the key balance in the energy equation as follows. Let the temperature disturbance be denoted by $\tilde{T}$. The unsteady term $\partial\tilde{T}/\partial t = O(\epsilon^{-2}\tilde{T})$ while the spanwise advection $w\partial T_{3b}/\partial z =$

$O(\epsilon\epsilon_d \cdot \epsilon^{-3})$, and so the balance of the two suggests that $\tilde{T} = O(\epsilon_d)$. The associated density disturbance of the same order-of-magnitude would then appear at the leading-order expansion of the continuity equation. Substituting (3.5)–(3.7*a*,*b*) into the NS equations, we obtain the equations governing the lower-deck normal-mode disturbance,

$$-\mathrm{i}\omega\hat{\rho}_3 + \rho_w\left(\mathrm{i}\alpha\hat{u}_3 + \frac{\partial\hat{v}_3}{\partial y_3} + \frac{\partial\hat{w}_3}{\partial Z}\right) + \mathrm{i}\alpha\lambda_u y_3\hat{\rho}_3 + \frac{\partial\rho_w}{\partial Z}\hat{w}_3 = 0, \tag{3.8}$$

$$\rho_w\left(-\mathrm{i}\omega\hat{u}_3 + \mathrm{i}\alpha\lambda_u y_3\hat{u}_3 + \lambda_u\hat{v}_3 + \lambda_{uZ}y_3\hat{w}_3\right) = -\mathrm{i}\alpha\hat{p}_3 + \mu_w\frac{\partial^2\hat{u}_3}{\partial y_3^2} + \lambda_u\frac{\partial\hat{\mu}_3}{\partial y_3}, \tag{3.9}$$

$$\frac{\partial\hat{p}_3}{\partial y_3} = 0, \quad \rho_w\left(-\mathrm{i}\omega\hat{w}_3 + \mathrm{i}\alpha\lambda_u y_3\hat{w}_3\right) = -\frac{\partial\hat{p}_3}{\partial Z} + \mu_w\frac{\partial^2\hat{w}_3}{\partial y_3^2}, \tag{3.10a,b}$$

$$\rho_w\left(-\mathrm{i}\omega\hat{T}_3 + \mathrm{i}\alpha\lambda_u y_3\hat{T}_3 + \frac{\partial T_w}{\partial Z}\hat{w}_3\right) = \mu_w\frac{\partial^2\hat{T}_3}{\partial y_3^2}, \tag{3.11}$$

while the expansion of Chapman's viscosity law yields

$$\hat{\mu}_3 = \frac{\partial\mu}{\partial\bar{y}_3}(0)\hat{T}_3 = \hat{T}_3. \tag{3.12}$$

It is worth pointing out that (3.8)–(3.11) remain valid for a general viscosity law, but (3.12) would be different. The present instability exhibits two significantly distinct features from those of usual T-S or first Mack modes (Smith 1979*b*, 1989). The temperature/density fluctuation is of $O(\epsilon_d)$, much stronger than the $O(\epsilon\epsilon_d)$ velocity fluctuation. As a result, the temperature/density and velocity fields are coupled, i.e. the disturbance in the lower deck is fully compressible as opposed to the incompressible dynamics of first Mack modes. Instability with such an asymptotic structure does not appear to have been identified before. Governed by partial differential equations, the instability is of a bi-global nature. Interestingly and remarkably, the system can be reduced to a one-dimensional eigenvalue problem in the spanwise direction, which amounts to a substantial simplification (cf. Kátai & Wu 2020). The ensuing algebra may appear rather complex. The end result is (3.21), which along with (3.25*a–c*) will form the eigenvalue problem. Readers uninterested in the derivation may go directly to (3.21).

The lower-deck velocities and temperature can, despite being coupled, be solved in terms of the pressure by following earlier papers (Smith 1979*a*; Walton & Patel 1998; Kátai & Wu 2020). In order to simplify (3.8)–(3.11), we first introduce the rescaled variable

$$\zeta = (\mathrm{i}\alpha\lambda_u\rho_w/\mu_w)^{1/3}\,y_3 + \zeta_0, \quad \zeta_0 = -\,(\mathrm{i}\alpha\lambda_u\rho_w/\mu_w)^{1/3}\,\omega/(\alpha\lambda_u). \tag{3.13a,b}$$

The z-momentum equation (3.10*a*,*b*) is then reduced to an inhomogeneous Airy equation. The solution for $\hat{w}_3$, which satisfies the vanishing boundary and matching conditions, is found as

$$\hat{w}_3 = \frac{\pi}{\mu_w}\left(\frac{\mu_w}{\mathrm{i}\alpha\lambda_u\rho_w}\right)^{2/3}\frac{\partial\hat{p}_3}{\partial Z}\left(\frac{\mathrm{Gi}(\zeta_0)}{\mathrm{Ai}(\zeta_0)}\mathrm{Ai}(\zeta) - \mathrm{Gi}(\zeta)\right), \tag{3.14}$$

where $\mathrm{Ai}(\zeta)$ and $\mathrm{Gi}(\zeta)$ denote the Airy and Scorer functions, respectively. With $\hat{w}_3$ found, the temperature equation (3.11) amounts to an inhomogeneous Airy equation as well, and

the solution subject to vanishing matching and boundary conditions is obtained as

$$\hat{T}_3 = -\frac{\hat{T}_3^*(\zeta_0)}{\mathrm{Ai}(\zeta_0)}\mathrm{Ai}(\zeta) + \hat{T}_3^*(\zeta), \tag{3.15}$$

where

$$\hat{T}_3^*(\zeta) = \frac{\pi}{\mathrm{i}\alpha\lambda_u\mu_w}\left(\frac{\mu_w}{\mathrm{i}\alpha\lambda_u\rho_w}\right)^{1/3}\frac{\partial\hat{p}_3}{\partial Z}\frac{\partial T_w}{\partial Z}\left(\frac{\mathrm{Gi}(\zeta_0)}{\mathrm{Ai}(\zeta_0)}\mathrm{Ai}'(\zeta) - \mathrm{Gi}'(\zeta)\right), \tag{3.16}$$

with the prime representing the derivative with respect to ζ.

Differentiating (3.9) with respect to y_3 followed by using the continuity and energy equations (3.8) and (3.11), to eliminate $\hat{p}_3$, $\hat{v}_3$ and $\hat{T}_3$, (3.9) simplifies to

$$\frac{\partial^3\hat{u}_3}{\partial\zeta^3} - \zeta\frac{\partial\hat{u}_3}{\partial\zeta} = \frac{\lambda_{uZ}}{\mathrm{i}\alpha\lambda_u}\hat{w}_3 + \frac{\lambda_{uZ}}{\mathrm{i}\alpha\lambda_u}(\zeta-\zeta_0)\frac{\partial\hat{w}_3}{\partial\zeta} - \frac{1}{\mathrm{i}\alpha}\frac{\partial\hat{w}_3}{\partial Z}, \tag{3.17}$$

on which the boundary and matching conditions are imposed as

$$\hat{u}_3|_{\zeta=\zeta_0} = 0, \quad \left.\frac{\partial^2\hat{u}_3}{\partial\zeta^2}\right|_{\zeta=\zeta_0} = \left(\frac{\mu_w}{\mathrm{i}\alpha\lambda_u\rho_w}\right)^{2/3}\frac{\mathrm{i}\alpha\hat{p}_3}{\mu_w} - \left(\frac{\mu_w}{\mathrm{i}\alpha\lambda_u\rho_w}\right)^{1/3}\frac{\lambda_u}{\mu_w}\left.\frac{\partial\hat{T}_3}{\partial\zeta}\right|_{\zeta=\zeta_0}, \tag{3.18a,b}$$

$$\hat{u}_3|_{\zeta\to\infty} = A_1\lambda_u. \tag{3.19}$$

With $\hat{w}_3$ and $\hat{T}_3$ given by (3.14)–(3.15), the solution to (3.17)–(3.19) is found as

$$\hat{u}_3 = \phi_1\int_{\zeta_0}^{\zeta}\mathrm{Ai}(t)\,\mathrm{d}t + \phi_2\mathrm{Ai}(\zeta) + \phi_3\mathrm{Gi}(\zeta) + \phi_4\zeta\mathrm{Ai}'(\zeta) + \phi_5\zeta\mathrm{Gi}'(\zeta) - \phi_6, \tag{3.20}$$

where the expressions of ϕ_1-ϕ_6 are given in Appendix A. Inserting (3.20) into (3.19), we obtain the equation for $\hat{p}_3$,

$$\frac{\partial^2\hat{p}_3}{\partial Z^2} - \mathcal{R}(Z)\frac{\partial\hat{p}_3}{\partial Z} - \alpha^2\hat{p}_3 = \mathcal{Q}(Z)A_1, \tag{3.21}$$

which is an ordinary differential equation with respect to the spanwise variable Z. The functions $\mathcal{R}(Z)$ and $\mathcal{Q}(Z)$ have the expressions,

$$\left.\begin{aligned}\mathcal{R}(Z) = &\left(\frac{1}{4}\frac{\mu_{wZ}}{\mu_w} - \frac{1}{4}\frac{\rho_{wZ}}{\rho_w} + \frac{1}{2}\frac{\lambda_{uZ}}{\lambda_u}\right)\frac{\zeta_0}{\mathrm{Ai}(\zeta_0)}\left(\zeta_0\kappa(\zeta_0) + \mathrm{Ai}'(\zeta_0)\right)\\ &+\left(\frac{1}{4}\frac{\mu_{wZ}}{\mu_w} + \frac{3}{4}\frac{\rho_{wZ}}{\rho_w} + \frac{3}{2}\frac{\lambda_{uZ}}{\lambda_u}\right) + \left(1 + \frac{\mathrm{Ai}'(\zeta_0)}{\mathrm{Ai}^2(\zeta_0)}\kappa(\zeta_0)\right)\frac{\partial T_w}{\partial Z},\\ \mathcal{Q}(Z) = &(\mathrm{i}\alpha\lambda_u)^{5/3}\rho_w^{2/3}\mu_w^{1/3}\frac{\mathrm{Ai}'(\zeta_0)}{\kappa(\zeta_0)},\end{aligned}\right\} \tag{3.22}$$

with

$$\kappa(\zeta_0) = \int_{\zeta_0}^{\infty}\mathrm{Ai}(t)\,\mathrm{d}t. \tag{3.23}$$

The reader is reminded that the main result (3.21) with (3.22) is derived under the assumption of Chapman's relation for viscosity. When the more accurate viscosity Sutherland's law is adopted, (3.21) can still be derived, but the expressions for $\mathcal{R}(Z)$ and $\mathcal{Q}(Z)$ would differ from (3.22).

3.3. *Upper deck*

Similar to the first mode (Smith 1989), the wall-normal velocity at the outer edge of the main layer acts on the upper deck to generate a pressure perturbation, which acts in turn on the viscous lower deck. It thus suffices to consider the pressure of the modal disturbance in the upper deck, where the pressure expands as

$$p = \epsilon^2 \epsilon_x^{5/3} \bar{p}_1 + \epsilon^2 \epsilon_d \hat{p}_1 E. \tag{3.24}$$

The equation governing the pressure disturbance and the matching conditions are

$$\alpha^2 \left(M_\infty^2 - 1\right) \hat{p}_1 + \frac{\partial^2 \hat{p}_1}{\partial y_1^2} + \frac{\partial^2 \hat{p}_1}{\partial Z^2} = 0, \quad \left.\frac{\partial \hat{p}_1}{\partial y_1}\right|_{y_1=0} = -\alpha^2 A_1, \quad \hat{p}_1|_{y_1=0} = \hat{p}_3(Z). \tag{3.25a–c}$$

The instability of the heating-induced streaky flow is governed by (3.25*a–c*) and (3.21). Note that the coefficients are only related to the wall shear $\lambda_u(Z)$ and wall temperature $T_w(Z)$, indicating that the instability is, to leading-order accuracy, controlled by λ_u and T_w only.

3.4. *The eigenvalue problem*

Since the coefficients of (3.21) are periodic functions of Z with spanwise number β (see (2.37)–(2.38*a*,*b*)), we use Floquet theory to express $\hat{p}_1$, $\hat{p}_3$ and A_1 in the form

$$\{\hat{p}_1(y_1, Z), \hat{p}_3(Z), A_1(Z)\} = \exp(\mathrm{i}q\beta Z) \sum_{n=-\infty}^{\infty} \{\bar{p}_n(y_1), \bar{P}_n, \bar{A}_n\} \exp(\mathrm{i}n\beta Z), \tag{3.26}$$

where q is the Floquet exponent, which is taken to be real-valued since the disturbance is bounded in the spanwise direction. Substitution of (3.26) into (3.25*a–ca*) yields

$$\frac{\partial^2 \bar{p}_n}{\partial y_1^2} - \left[(n+q)^2\beta^2 - \alpha^2(M_\infty^2 - 1)\right]\bar{p}_n = 0. \tag{3.27}$$

Let $\Lambda = (n+q)^2\beta^2 - \alpha^2(M_\infty^2 - 1)$, whose real part is denoted by Λ_r. Typically, α_r turns out to be significantly greater than α_i numerically, and so the far-field behaviour of $\bar{p}_n$ is dominated by Λ_r. The solution satisfying (3.25*a–cc*) is found as

$$\bar{p}_n = \bar{P}_n \exp(-\Lambda^{1/2} y_1) \quad \text{if } \Lambda_r > 0, \quad \bar{p}_n = \bar{P}_n \exp(-\mathrm{i}(-\Lambda)^{1/2} y_1) \quad \text{if } \Lambda_r < 0; \tag{3.28a,b}$$

here we dismiss the branch that becomes exponentially large in the far field when $\Lambda_r > 0$, while for $\Lambda_r < 0$, the branch corresponding to a negative group velocity in the wall-normal direction is dismissed on physical grounds. Equation (3.28*b*) indicates that due to spanwise-periodic heating, instability modes may emit acoustic waves to the far field while attenuating slowly, the rate of which is controlled by α_i. When the mode is neutral, the disturbance is purely oscillatory in the far field, in contrast to non-radiating first Mack modes. Substitution of (3.28*a*) or (3.28*b*) into (3.25*b*) yields the pressure-displacement relation

$$\bar{A}_n = \alpha^{-2} \mathcal{L}_n(\alpha) \bar{P}_n, \tag{3.29}$$

where $\mathcal{L}_n(\alpha) = \Lambda^{1/2}$ for $\Lambda_r > 0$, while $\mathcal{L}_n(\alpha) = \mathrm{i}(-\Lambda)^{1/2}$ for $\Lambda_r < 0$.

4. Numerical analysis and results

4.1. *Dispersion relation*

In order to solve the eigenvalue problem, (3.21) and (3.29), which is one dimensional in the spanwise direction, we express $\mathcal{R}(Z)$ and $\mathcal{Q}(Z)$ in (3.21) as Fourier series

$$\mathcal{R}(Z) = \sum_{l=-\infty}^{\infty} R_l \, \mathrm{e}^{\mathrm{i}l\beta Z}, \quad \mathcal{Q}(Z) = \sum_{l=-\infty}^{\infty} Q_l \, \mathrm{e}^{\mathrm{i}l\beta Z}. \tag{4.1a,b}$$

Equating the coefficients of the respective Fourier components, we obtain an infinite-dimensional system for $\bar{P}_n$, which is truncated to $[-N, N]$ and written in the matrix form

$$\boldsymbol{M}\bar{\boldsymbol{P}} = \boldsymbol{0}, \quad \bar{\boldsymbol{P}} = (\bar{P}_{-N}, \bar{P}_{-N+1}, \ldots, \bar{P}_0, \ldots, \bar{P}_N)^{\mathrm{T}}, \tag{4.2a,b}$$

where $\boldsymbol{M} = \boldsymbol{M_1}(\alpha, \beta, q) + \boldsymbol{M_2}(\alpha, \beta, \omega, q, \lambda_u, T_w)$, with $\boldsymbol{M_1}$ being a diagonal matrix and $\boldsymbol{M_2}$ a full matrix,

$$(\boldsymbol{M_1})_{n,n} = \alpha^2 + \beta^2(q+n)^2, \quad (\boldsymbol{M_2})_{n,j} = \mathrm{i}\beta(j+q)R_{n-j} + \alpha^{-2}\mathcal{L}_n Q_{n-j}. \tag{4.3a,b}$$

For (4.2a,b) to have non-zero solutions, the determinant of matrix $\boldsymbol{M}$ must vanish, namely,

$$\mathcal{D}(\alpha) = \det\left(\boldsymbol{M}(\alpha, \beta, \omega, q, \lambda_u, T_w)\right) = 0, \tag{4.4}$$

which is the dispersion relation. In the limiting case where the heating is absent or negligible (i.e. $h = 0$ in (2.37)), $\lambda_u = 1$, we have $R_l = 0 \ \forall l$, and $Q_l = 0 \ \forall l \neq 0$. The relation (4.4) simplifies to

$$\mathcal{D}(\alpha) = \alpha^2\left(\alpha^2 + \beta^2(q+K)^2\right)\kappa(\zeta_0) + (\mathrm{i}\alpha)^{5/3}\,\rho_w^{2/3}\mu_w^{1/3}\mathcal{L}_K \mathrm{Ai}'(\zeta_0) = 0, \tag{4.5}$$

where $\kappa(\zeta_0)$ is given in (3.23). For any integer K, this is the dispersion relation for first Mack modes with spanwise wavenumber $\beta_{TS} = \beta(q+K)$ (Smith 1989).

4.2. *Growth rates*

The streaky flow induced by surface temperature distribution (2.37)–(2.38a,b) with $h = 1$, $d = 0.5$ and $\beta = 2\pi$ was calculated in § 2 for $M_\infty = 3$, and we now consider the impact of the heating on linear stability. The eigenvalue problem is solved starting from a position far upstream where the effect of heating is negligible so that the value of α for the first Mack mode, obtained by solving (4.5), is taken as the first guess in Muller's iteration (Muller 1956). At subsequent streamwise locations, the convergent value of α for the previous location is used as an initial guess to find the root of the dispersion relation (4.4). The tolerance is taken to be 10^{-10}. Resolution checks were performed, and it was found that the results with the Fourier series truncated at $N = 7$, 15 and 31 exhibit no difference to the graphical precision; the relative errors between the two resolutions ($N = 15$ and 7) are $O(10^{-6})$, and the relative errors between $N = 15$ and 31 reduced to be no greater than 10^{-10}, the level of tolerance. The rapid convergence with respect to N is due to the simple sinusoidal distribution of the surface temperature $T_w(Z)$ and wall shear $\lambda_u(Z)$. A larger N is likely required for a more complex spanwise distribution (cf. Kátai & Wu 2020).

In figure 4 we show in the α–ω plane the growth rates of instability modes with different spanwise wavenumbers for $\lambda_u(Z)$ being calculated for surface temperature distribution (2.38a,b) with (2.39). Different lines refer to different streamwise locations between $\bar{X} = -1.2$ (thick solid lines) and $\bar{X} = 0$ (thick dotted lines) with an increment of 0.05.

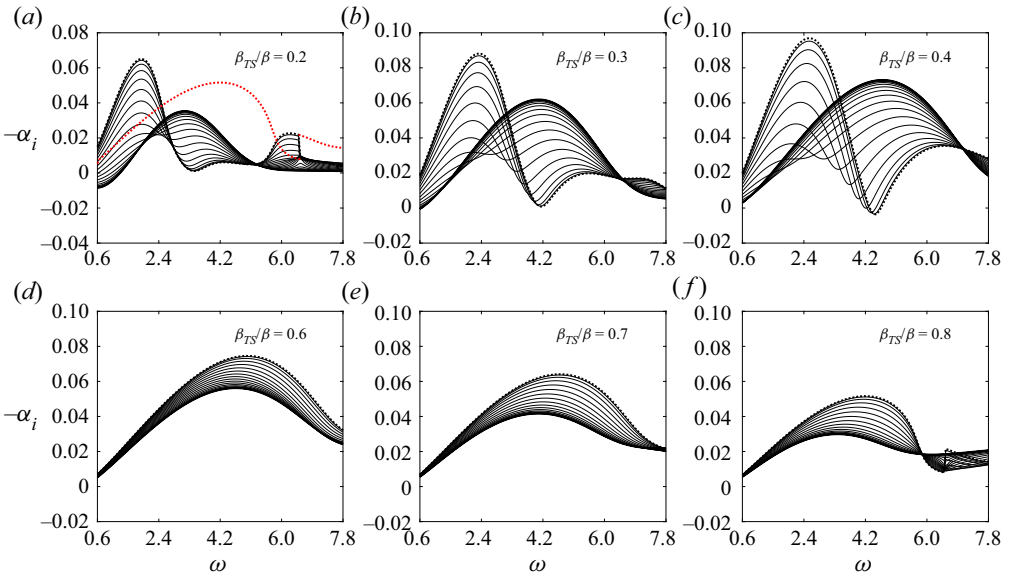

Figure 4. Growth rates vs the frequency ω at various streamwise locations $\bar{X}$ for $S(Z) = \cos(2\pi Z)$. Thick solid lines: $\bar{X} = -1.2$; thick dotted lines: $\bar{X} = 0$. Different lines in between refer to different streamwise locations with an increment of 0.05. The red dotted lines represent the continuation of the mode to the right/left by increasing/descreasing ω for fixed $\bar{X} = 0$.

The thick solid lines can be considered as representing the growth rates of first Mack modes. Due to the local nature of the instability problem as well as the symmetry of the wall temperature (2.37) and the wall shear (2.40), it suffices to calculate only the upstream half of the heating region. Six representative spanwise wavenumbers ($\beta_{TS}/\beta = 0.2$, 0.3, 0.4, 0.6, 0.7 and 0.8) are chosen. For weakly three-dimensional modes with $\beta_{TS} < 0.5\beta$ (figures 4*a–c*), there is always a range of frequencies in which the growth rate ($-\alpha_i$) of instability modes decreases monotonically from the upstream to the centre of the elements. For example, for $\beta_{TS}/\beta = 0.3$, a stabilising effect occurs for $4 < \omega < 6$. For sufficiently low and high frequencies, the growth rate increases monotonically. Between the low and intermediate frequencies, the growth rate varies non-monotonically. However, for strongly three-dimensional modes with $\beta_{TS} > 0.5\beta$, figures 4(*d–f*) show that the growth rate ($-\alpha_i$) increases monotonically with $\bar{X}$ for almost all frequencies with the exception for high values in figure 4(*f*), and the heating elements play a broad destabilising role. Non-continuous variations of the growth rate ($-\alpha_i$) with the frequency ω can be observed for high frequencies in figures 4(*a*,*f*). Such discontinuities will be discussed later.

As in Kátai & Wu (2020), for $\beta_{TS}/\beta = 0.5$ (i.e. $q = 0.5$), we have also identified antisymmetric and symmetric modes, whose eigenfunctions $\hat{p}_3(Z)$ are odd and even functions of Z, respectively, and their growth rates are shown in figure 5(*a*,*b*). The instability characteristics of these antisymmetric/symmetric modes are similar to that of weakly/strongly three-dimensional modes in figure 4, and can be regarded as the continuation of the latter, respectively. The spanwise distributions of the lower-deck pressure $\hat{p}_3(Z)$ of these modes, which are also referred to as subharmonic modes, are displayed in figure 6(*a*,*b*). In addition to $q = 1/2$, antisymmetric/symmetric modes are also found for $q = k/2$ with $k = 2, 3, \ldots$. Of these, $q = 1$ ($k = 2$) represents fundamental parametric resonance. Different from the subharmonic ones, figure 5(*c*,*d*) shows nearly the same variation (increase) of the growth rates for antisymmetric and symmetric

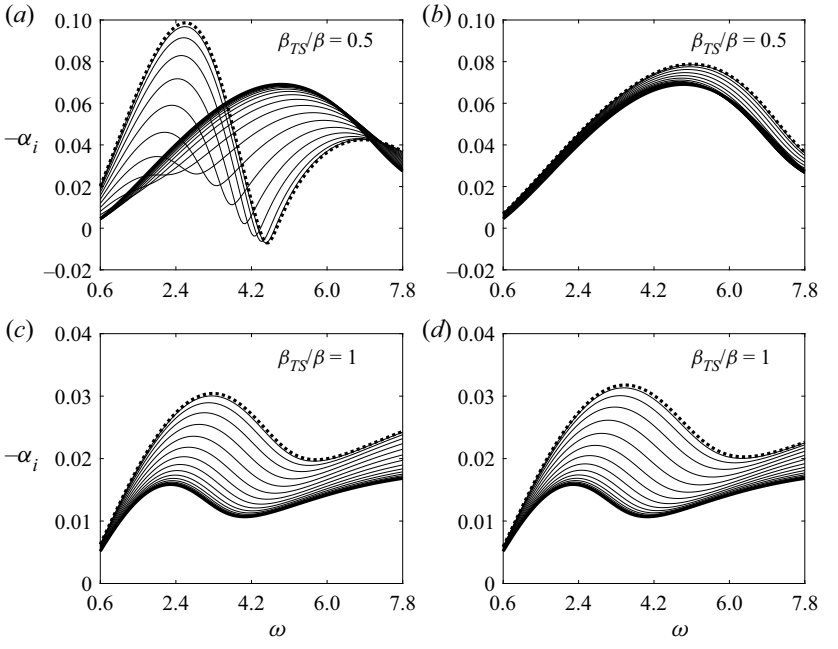

Figure 5. Growth rates vs the frequency ω of subharmonic (a,b) and fundamental modes (c,d): (a,c) antisymmetric modes; (b,d) symmetric modes. Thick solid lines: $\bar{X} = -1.2$; thick dotted lines: $\bar{X} = 0$. Different lines in between refer to different streamwise locations with an increment of 0.05.

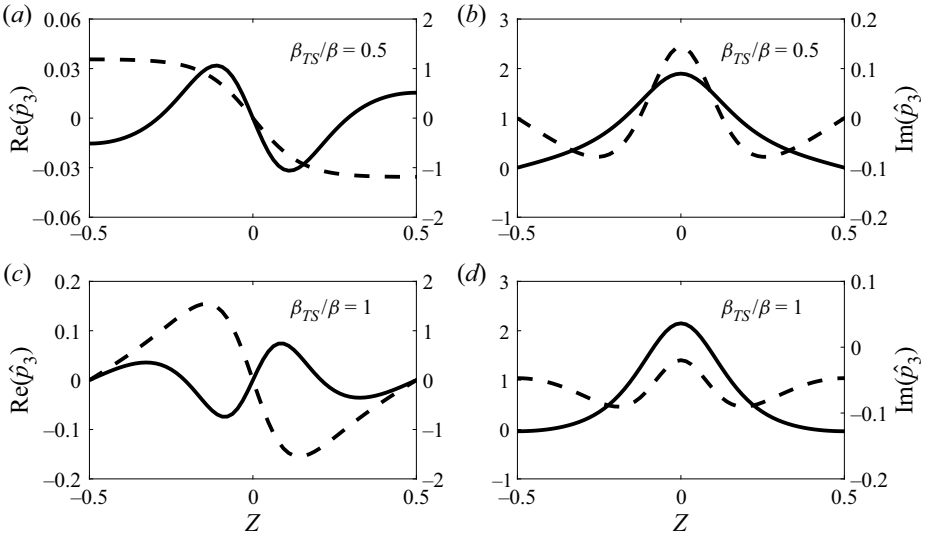

Figure 6. Spanwise shapes $\hat{p}_3(Z)$ of symmetric (b,d) and antisymmetric (a,c) modes at $\bar{X} = 0$ with $\omega = 3$: (a,b) subharmonic modes; (c,d) fundamental modes.

fundamental modes. The corresponding spanwise distributions of the pressure $\hat{p}_3(Z)$ are presented in figure 6(c,d).

Calculations are carried out also for heating elements with larger spanwise spacing, corresponding to $\beta = \pi$. The growth rates are displayed in figure 7. Compared with the

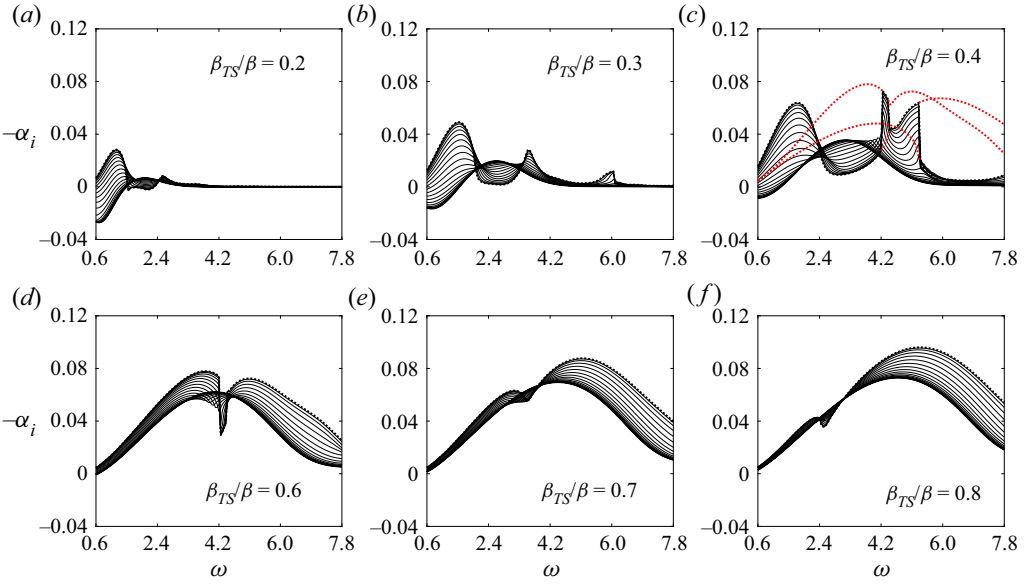

Figure 7. Growth rates vs the frequency ω at various streamwise locations $\bar{X}$ for $S(Z) = \cos(\pi Z)$. Thick solid lines: $\bar{X} = -1.2$; thick dotted lines: $\bar{X} = 0$. Different lines in between refer to different streamwise locations with an increment of 0.05. The red dotted lines represent the continuation of the mode to the right/left by increasing/descreasing ω for fixed $\bar{X} = 0$.

case of $\beta = 2\pi$ shown in figure 4, the instability characteristics are broadly similar, but appreciable differences arise. For example, for $\beta_{TS} = 0.4\beta$ (figure 7*b*), a distinctive band of high-frequency Mack modes are destabilised to become as dominant as destabilised low-frequency modes, and this band is marked by non-continuous variations with the frequency. For $\beta_{TS} > 0.5\beta$, the modes within a small range of frequencies are stabilised by an amount that becomes rather moderate as β_{TS} increases.

A discussion of the discontinuities in figures 4 and 7 is in order. The discontinuities reflect coexistence of a multi-family of modes and 'mode crossing' phenomenon. The eigenvalue $\alpha(\omega, \bar{X})$ is a function of ω and $\bar{X}$. It can be calculated by using either of the two approaches: the first fixes $\bar{X}$ but varies ω gradually, and while the second fixes ω but increases $\bar{X}$ in small increments. The data in the figures were calculated by the latter approach. Each eigen mode so obtained evolves from an upstream first mode with a spanwise wavenumber $\beta_{TS} = (k + q)\beta$ with $0 \leq q \leq 1/2$, and, hence, each mode can be distinguished by (k, q), and be designated by $\alpha_{k,q}(\omega, \bar{X})$ with $k = 0, \pm 1, \ldots$, as shown by Kátai & Wu (2020). At each $\bar{X}$, these modes coexist and are intricately interlinked as $\bar{X}$ and ω vary. If k and q are fixed also, $\alpha_{k,q}(\omega, \bar{X})$ may not be a continuous function of ω. Taking $\bar{X} = 0$ as an example, a jump occurs at $\omega_c \approx 6.5$ as is shown figure 4(*a*), and the modes on both sides may be designated as $\alpha_{0,0.2}(\omega, \bar{X})$, which evolves from a first mode upstream with $\beta_{TS} = 0.2\beta$. On the other hand, with $\bar{X} = 0$ being fixed, the mode to the left of the jump with $\omega < \omega_c$ may be continued parametrically to the right by gradually increasing ω, and similarly, the mode to the right of the jump with $\omega > \omega_c$ may be continued to the left by decreasing ω. The results are indicated by the red dotted lines. Interestingly, these extended lines turned out to coincide with the dotted lines in figure 4(*f*), and the jumps in figure 4(*a*,*f*) overlap. As each mode on the dotted lines in figure 4(*f*) develops from an upstream first mode with $\beta_{TS} = (-1 + 0.2)\beta$, it is designated as $\alpha_{-1,0.2}(\omega, \bar{X})$ and so

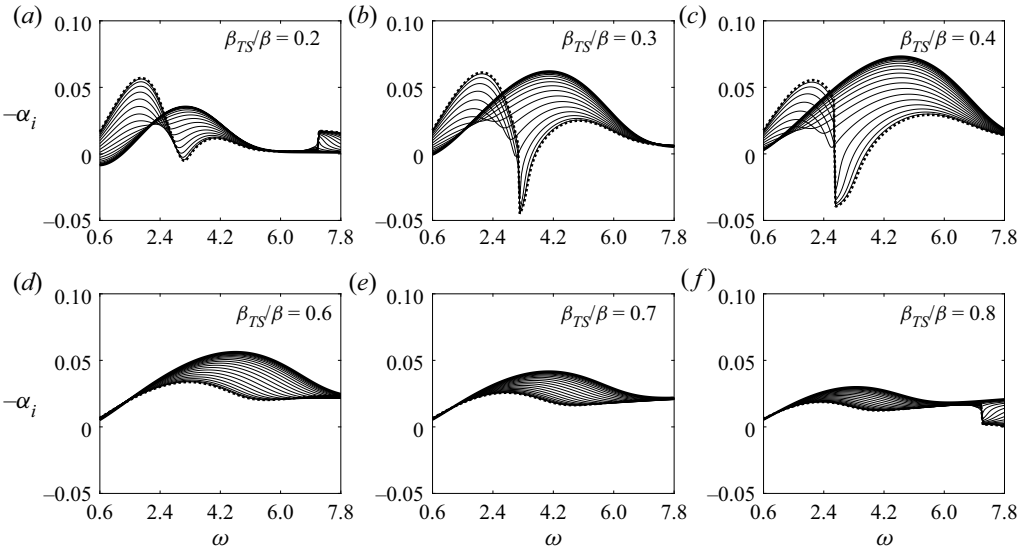

Figure 8. Growth rates vs the frequency ω at various streamwise locations $\bar{X}$ for $S(Z) = 0.5 + \cos(2\pi Z)$. Thick solid lines: $\bar{X} = -1.2$; thick dotted lines: $\bar{X} = 0$. Different lines in between refer to different streamwise locations with an increment of 0.05.

is the mode on the red extended lines in figure 4(*a*). Indeed, starting with a mode on this line, we can trace it back to an upstream first mode with $\beta_{TS}/\beta = 0.8$. It follows that as ω crosses ω_c, there is a crossover from $\alpha_{0,0.2}(\omega, \bar{X})$ to $\alpha_{-1,0.2}(\omega, \bar{X})$ despite the fact they are on the same smooth line.

The jumps in figure 7(*c*,*d*) are associated with similar crossovers of modes. Again take $\bar{X} = 0$ for illustration. The discontinuous dotted curve represents the mode $\alpha_{0,0.4}(\omega, \bar{X})$. The small segment between the two jumps on the left can be continued to the smaller and larger ω, whilst the dotted line to the left of the first jump is continued to the right (to connect with $\alpha_{0,0.4}(\omega, \bar{X})$). The extended lines turn out to be the same as the three segments of the dotted line in figure 7(*d*), and, thus, represent the mode $\alpha_{-1,0.4}(\omega, \bar{X})$, which evolves from an upstream first mode with $\beta_{TS} = (-1 + 0.4)\beta$. Similarly, the dotted lines to the right/left of the third jump in figure 7(*c*) can also be continued to the left/right, respectively. The resulting extended lines represent the mode $\alpha_{1,0.4}(\omega, \bar{X})$, which develops from an upstream first mode with $\beta_{TS} = (1 + 0.4)\beta$ (not shown).

Figure 8 displays the results for the heating elements with spanwise distribution $S(Z)$ given in (2.38*a*,*b*) with $s_0 = 0.5$, $s_1 = 1$ and $s_n = 0$ for all $n \leq 2$, that is,

$$S(Z) = 0.5 + \cos(2\pi Z), \tag{4.6}$$

which combines a spanwise uniform part with a simple spanwise-harmonic Fourier component. Stabilising effects can be observed for most cases except low-frequency modes for $\beta_{TS}/\beta < 0.5$ plus a band of high-frequency modes for $\beta_{TS}/\beta = 0.2$. Comparing figure 8 with figure 4, one notes that the addition of the spanwise uniform component leads to an opposite effect for the modes with $\beta_{TS}/\beta > 0.5$, whose growth rates are substantially reduced, while for modes $\beta_{TS}/\beta < 0.5$, the effect remains similar but quantitatively the combined spanwise uniform and periodic heating causes a stronger stabilising effect. These results indicate the possibility of inhibiting/enhancing first Mack modes via a suitable combination of Fourier components in the spanwise distribution $S(Z)$.

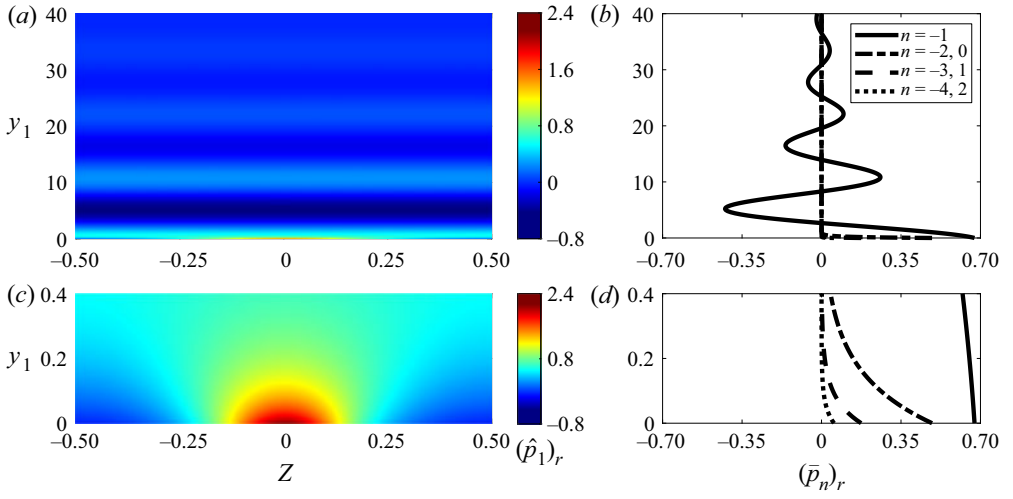

Figure 9. Distributions of $(\hat{p}_1)_r$ and corresponding Fourier components $(\bar{p}_n)_r$ at $\bar{X} = 0$ for a radiating mode with $\omega = 3$ and $\beta_{TS}/\beta = 1$: (*a*,*c*) contours of $(\hat{p}_1)_r$; (*b*,*d*) profiles of $(\bar{p}_n)_r$ for several values of n.

4.3. *Distribution of eigenfunctions*

The eigenfunction distributions in the upper and lower decks are of interest as they project distinctive features of the instability modes. Figure 9(*a*) displays the distribution of the upper-deck pressure at $\bar{X} = 0$ of a radiating mode with $\omega = 3$ and $\beta_{TS}/\beta = 1$ for the spanwise distribution $S(Z) = \cos(2\pi Z)$. Only the real part, $(\hat{p}_1(y_1, Z))_r$, is shown since the distribution of the imaginary part looks similar. As is illustrated, the mode radiates an acoustic wave to the far field while undergoing slow attenuation, which is controlled by α_i. The profiles of several low-order Fourier components $(\bar{p}_n(y_1))_r$ are shown in figure 9(*b*), where $n = -1$ represents the radiating component while other components rapidly attenuate exponentially in the region $y_1 = O(1)$ as shown in figure 9(*c*,*d*). That the $n = -1$ component emits a sound wave is indicated by (3.28*b*). For an integer β_{TS}/β, there is at least one value $n = -q$ ensuring $\Lambda_r < 0$, and so the $n = -1$ component is radiating for modes with $\beta_{TS}/\beta = 1$ (i.e. $q = 1$ and $K = 0$). It is worth noting that the growth rate of the mode shown is rather significant. For modes with reduced growth rates, the radiating character becomes even more prominent (see figure 12). These modes are fundamentally different from the radiating modes identified in high enthalpy boundary layers over a cooled wall (Mack 1984; Chuvakhov & Fedorov 2016).

Figure 10 displays the contours of the temperature and velocity disturbances in the y_3–Z plane at three streamwise locations, $\bar{X} = -1$, -0.5 and 0, for a mode with $\omega = 4$ and $\beta_{TS}/\beta = 0.3$; again, only the real parts, $(\hat{T}_3(y_3, Z))_r$ and $(\hat{u}_3(y_3, Z))_r$, are shown as representatives. One notes that $(\hat{T}_3)_r$ (left column) and $(\hat{u}_3)_r$ (right column) feature double- and single-deck structures, respectively. From the upstream to the centre of the elements, $(\hat{T}_3)_r$ and $(\hat{u}_3)_r$ exhibit qualitatively similar characters, but they both become progressively more concentrated in the spanwise direction with their maxima and minima moving closer to the centreline. This mode exhibits no symmetry about $Z = 0$. Contours of the eigenfunction of a symmetric radiating mode with $\omega = 3$ and $\beta_{TS}/\beta = 1$ are shown in figure 11. A comparison with figure 10 reveals a number of differences between the eigenfunction contours of symmetric and asymmetric modes. The temperature contours of the present symmetric mode again feature two decks of cells, but the cells in each deck

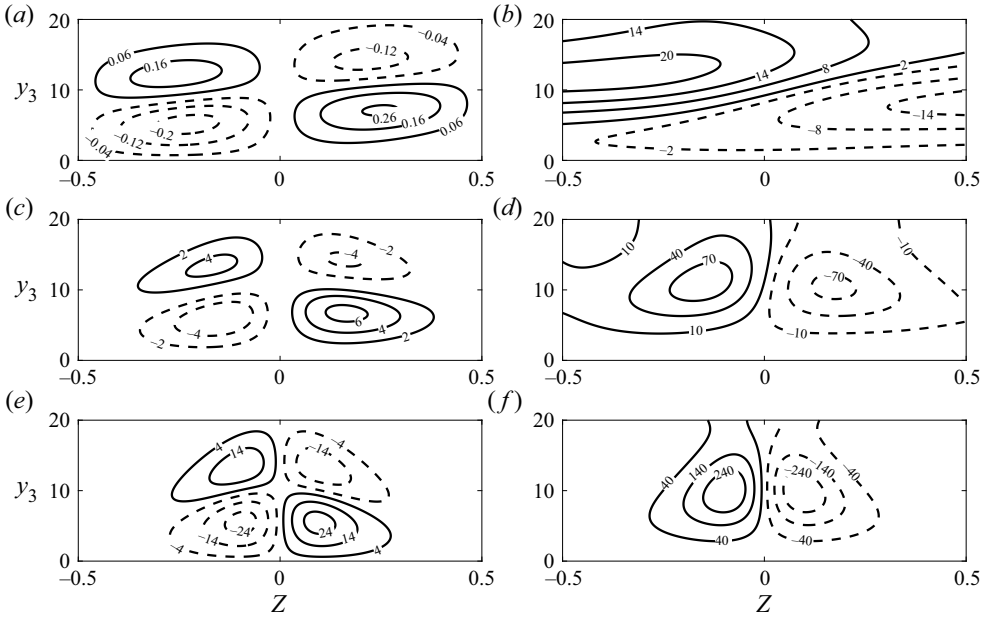

Figure 10. Contours of $(\hat{T}_3)_r$ (a,c,e) and $(\hat{u}_3)_r$ (b,d,f) for $\omega = 4$ and $\beta_{TS}/\beta = 0.3$ at three locations $\bar{X} = -1$ (a,b), -0.5 (c,d) and 0 (e,f). Solid and dashed lines represent contours of positive and negative values.

remain of the same sign, in contrast to the alternating signs of $(\hat{T}_3)_r$ for an asymmetric mode. Within one spanwise wavelength, contours of $(\hat{u}_3)_r$ consist of three cells with the central cell being flanked symmetrically by two side ones.

Figures 12 and 13 display the eigenfunction distributions respectively in the upper and lower decks of the mode with $\omega = 3$ and $\beta_{TS}/\beta = 1$ for the spanwise heating distribution (4.6); the parameters are otherwise the same as those in figures 9 and 11. Figure 12 indicates a more prominent acoustic radiation than that shown in figure 9. As explained earlier, this is due to the fact that the growth rate is reduced by the stabilising effect of heating in this case. Contours of the real parts of disturbance temperature and velocity, $(\hat{T}_3(y_3, Z))_r$ and $(\hat{u}_3(y_3, Z))_r$, are broadly similar to those in figure 11.

5. Summary and conclusions

In this paper we have investigated the impact of streamwise-elongated, spanwise-periodic surface heating on supersonic first Mack modes, whose streamwise and spanwise wavelengths are both of $O(Re^{-3/8}L)$, which is on the triple-deck scale. We take the spanwise length scale of the heating elements to be of this order, but the streamwise length scale is assumed to be much longer. A simplified system governing the heating-induced streaky flow is then deduced. When Chapman's viscosity law is employed, a remarkably simple similarity solution is found in terms of the Dorodnitsyn–Howarth variable.

In the presence of spanwise-periodic heating elements, the linear stability of the streaky flow is fully compressible in the lower deck with the disturbance temperature and velocity being coupled. The instability is bi-global in its nature. For the viscous instability on the triple-deck scale, this bi-global stability is simplified to a one-dimensional eigenvalue

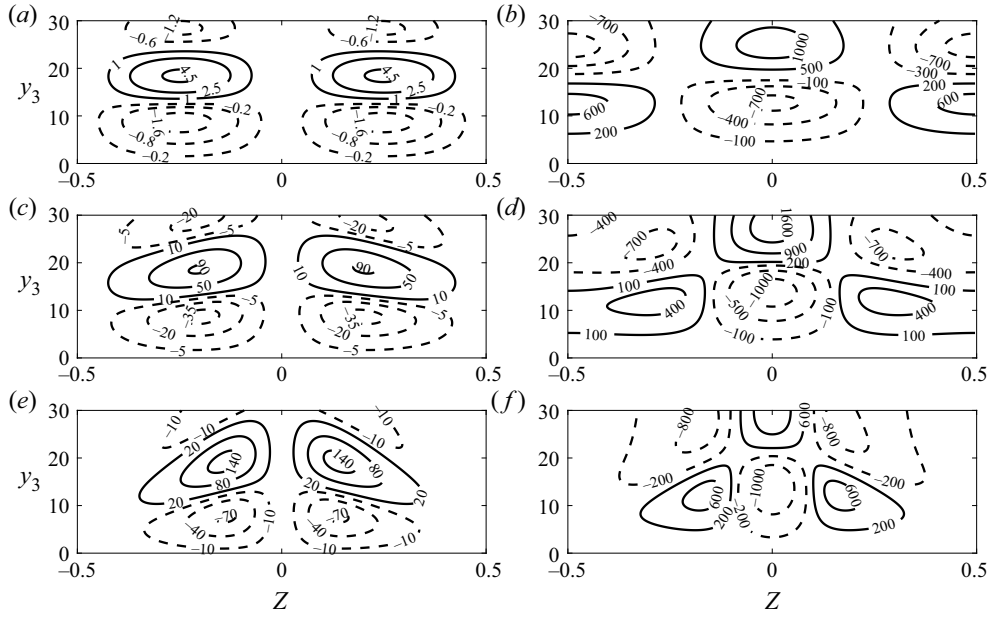

Figure 11. Contours of $(\hat{T}_3)_r$ (a,c,e) and $(\hat{u}_3)_r$ (b,d,f) for a symmetric mode with $\omega = 3$ and $\beta_{TS}/\beta = 1$ at three locations $\bar{X} = -1$ (a,b), -0.5 (c,d) and 0 (e,f). Solid and dashed lines represent contours of positive and negative values.

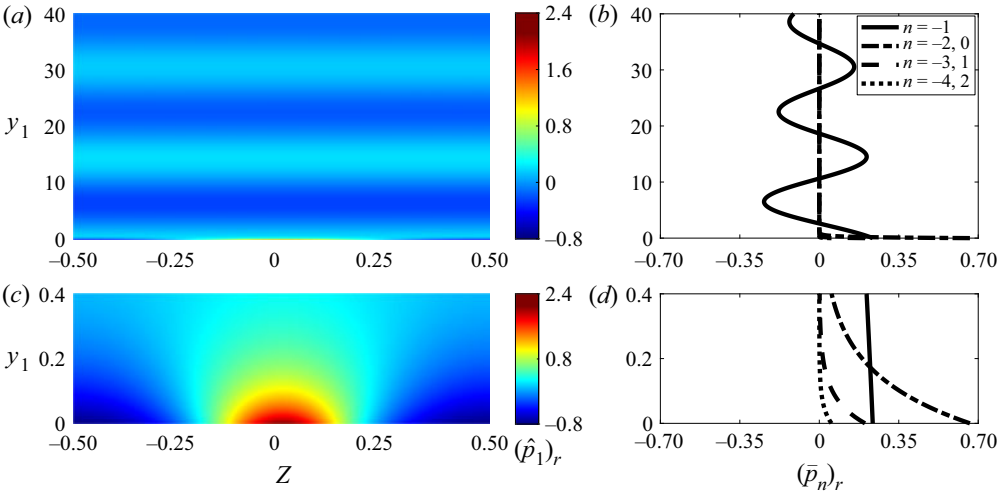

Figure 12. Distributions of $(\hat{p}_1)_r$ and corresponding Fourier components $(\bar{p}_n)_r$ at $\bar{X} = 0$ for a radiating mode with $\omega = 3$ and $\beta_{TS}/\beta = 1$ when heating is of form (4.6): (a,c) contours of $(\hat{p}_1)_r$; (b,d) profiles of $(\bar{p}_n)_r$ for several values of n.

problem in the spanwise direction. Moreover, the instability is shown to be controlled by the spanwise-dependent wall shear λ_u and wall temperature T_w only. With T_w prescribed and λ_u obtained analytically from the similarity solution, it was possible to omit the calculation of the streaky flow and focus on the instability directly, which may be considered as the continuation of upstream first Mack modes into the streaky region.

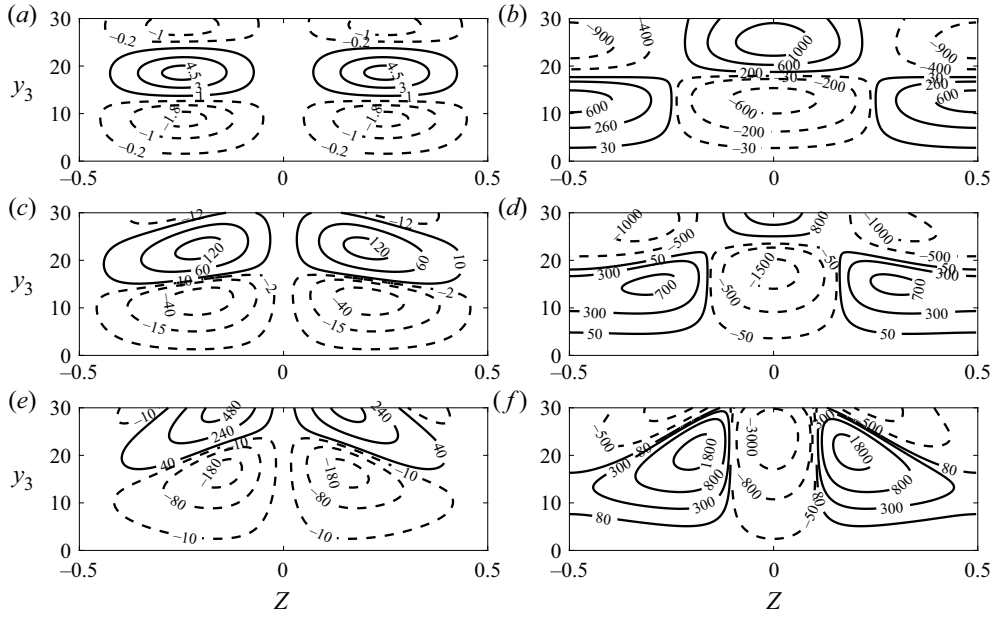

Figure 13. Contours of $(\hat{T}_3)_r$ (a,c,e) and $(\hat{u}_3)_r$ (b,d,f) for $\omega = 3$ and $\beta_{TS}/\beta = 1$ at three locations $\bar{X} = -1$ (a,b), -0.5 (c,d) and 0 (e,f) when heating is of form (4.6). Solid and dashed lines represent contours of positive and negative values.

The asymptotic approach provides an efficient tool to predict the surface-heating-induced streaky flow, and further to quantify the effect of heating on linear stability. Equally importantly, it reveals *a priori* the distinctive characteristics of the instability, namely, strong temperature perturbation within the boundary layer and spontaneous radiation of an acoustic wave to the far field.

The reduced eigenvalue problem was solved numerically for an array of spanwise-periodic heating elements whose streamwise and spanwise distributions are taken to be Gaussian and cosine, respectively. Heating of this form stabilises weakly three-dimensional modes in a range of frequencies. Outside of this band, the effect is opposite. For strongly three-dimensional modes, an appreciable destabilising effect is observed for almost all frequencies. Calculations are performed also for the heating elements with a different spanwise distribution which combines spanwise uniform and sinusoidal Fourier components. Apart from the low-frequency modes and high-frequency weakly three-dimensional modes, stabilising effects are found for the heating with this spanwise combination. These results, pertinent to some simplest spanwise distributions of heating, suggest that it is possible to suppress/enhance transition by using this simple active control technique. The required stabilising/destabilising effects may be achieved and optimized by a suitable combination of the Fourier components in the spanwise distribution of the heating source. The destabilising effect might be exploited in scramjet combustor to expedite transition and thereby enhance mixing.

It should be pointed out here that the numerical results summarised above are limited to supersonic flows of moderate Mach number where Chapman's viscosity law is valid. Furthermore, the ratio of the streamwise and spanwise length scales of the heating elements is assumed to be no greater than $Re^{3/8}$. It is necessary to extend the analysis and calculations to a more accurate (e.g. Sutherland's) law for viscosity and/or to heating

elements which are more elongated than assumed here. Work on these aspects is in progress.

Acknowledgements. The authors would like to thank the reviewers for their comments and suggestions, which have helped us improve the presentation and content of the paper.

Funding. This work was supported by NSFC (grant no. 91952202).

Declaration of interests. The authors report no conflict of interest.

Author ORCIDs.
Kaixin Zhu https://orcid.org/0000-0002-9450-9662;
Xuesong Wu https://orcid.org/0000-0002-3406-8017.

Appendix A

The expressions of ϕ_1–ϕ_6 in (3.20) are found as

$$\left.\begin{aligned}
\phi_1 &= \frac{1}{\mathrm{Ai}'(\zeta_0)}\left(\frac{\mu_w}{\mathrm{i}\alpha\lambda_u\rho_w}\right)^{2/3}\left(\frac{\mathrm{i}\alpha\hat{p}_3}{\mu_w}-\frac{1}{\mathrm{i}\alpha\mu_w^2}\frac{\partial\hat{p}_3}{\partial Z}\frac{\partial T_w}{\partial Z}\right)\\
&+\left(\frac{\mu_w}{\mathrm{i}\alpha\lambda_u\rho_w}\right)^{2/3}\frac{\pi}{\mathrm{i}\alpha\mu_w^2}\frac{\partial\hat{p}_3}{\partial Z}\frac{\partial_w}{\partial Z}\left(\frac{\mathrm{Gi}(\zeta_0)}{\mathrm{Ai}(\zeta_0)}\mathrm{Ai}'(\zeta_0)-\mathrm{Gi}'(\zeta_0)\right)-\frac{B_3\zeta_0^2}{4}\\
&-\frac{1}{\mathrm{Ai}'(\zeta_0)}\left(B_1\zeta_0\mathrm{Ai}(\zeta_0)+B_2\zeta_0\mathrm{Gi}(\zeta_0)+\frac{1}{4}B_4\zeta_0^2\mathrm{Gi}'(\zeta_0)+\frac{B_4-4B_2}{4\pi}\right),\\
\phi_2 &= B_1-\frac{3}{4}B_3,\quad \phi_3 = B_2-\frac{3}{4}B_4,\quad \phi_4=\frac{1}{4}B_3,\quad \phi_5=\frac{1}{4}B_4,\quad \phi_6=\frac{1}{3}B_5,
\end{aligned}\right\}\tag{A1}$$

where

$$\left.\begin{aligned}
B_1 &= \left(\frac{1}{3}\frac{\mu_{wZ}}{\mu_w}-\frac{1}{3}\frac{\rho_{wZ}}{\rho_w}+\frac{2}{3}\frac{\lambda_{uZ}}{\lambda_u}\right)\zeta_0\Gamma\frac{\partial\hat{p}_3}{\partial Z}\left(\frac{\mathrm{Gi}'(\zeta_0)}{\mathrm{Ai}(\zeta_0)}-\frac{\mathrm{Gi}(\zeta_0)\mathrm{Ai}'(\zeta_0)}{\mathrm{Ai}^2(\zeta_0)}\right)\\
&+\left(\frac{1}{3}\frac{\mu_{wZ}}{\mu_w}+\frac{2}{3}\frac{\rho_{wZ}}{\rho_w}+\frac{5}{3}\frac{\lambda_{uZ}}{\lambda_u}\right)\Gamma\frac{\partial\hat{p}_3}{\partial Z}\frac{\mathrm{Gi}(\zeta_0)}{\mathrm{Ai}(\zeta_0)}-\Gamma\frac{\partial^2\hat{p}_3}{\partial Z^2}\frac{\mathrm{Gi}(\zeta_0)}{\mathrm{Ai}(\zeta_0)},\\
B_2 &= -\left(\frac{1}{3}\frac{\mu_{wZ}}{\mu_w}+\frac{2}{3}\frac{\rho_{wZ}}{\rho_w}+\frac{5}{3}\frac{\lambda_{uZ}}{\lambda_u}\right)\Gamma\frac{\partial\hat{p}_3}{\partial Z}+\Gamma\frac{\partial^2\hat{p}_3}{\partial Z^2},\\
B_3 &= \left(\frac{1}{3}\frac{\mu_{wZ}}{\mu_w}-\frac{1}{3}\frac{\rho_{wZ}}{\rho_w}+\frac{2}{3}\frac{\lambda_{uZ}}{\lambda_u}\right)\Gamma\frac{\partial\hat{p}_3}{\partial Z}\frac{\mathrm{Gi}(\zeta_0)}{\mathrm{Ai}(\zeta_0)},\quad B_4=-B_3\frac{\mathrm{Ai}(\zeta_0)}{\mathrm{Gi}(\zeta_0)},
\end{aligned}\right\}\tag{A2}$$

with

$$\Gamma=\frac{\pi}{\mathrm{i}\alpha\mu_w}\left(\frac{\mu_w}{\mathrm{i}\alpha\lambda_u\rho_w}\right)^{2/3}.\tag{A3}$$

References

Aljohani, A.F. & Gajjar, J.S.B. 2017*a* Subsonic flow past localised heating elements in boundary layers. *J. Fluid Mech.* **821**, R2.

Aljohani, A.F. & Gajjar, J.S.B. 2017*b* Subsonic flow past three-dimensional localised heating elements in boundary layers. *Fluid Dyn. Res.* **49** (6), 065503.

Aljohani, A.F. & Gajjar, J.S.B. 2018 Transonic flow over localised heating elements in boundary layers. *J. Fluid Mech.* **844**, 746–765.

BRENNAN, G.S., GAJJAR, J.S.B. & HEWITT, R.E. 2021 Tollmien–Schlichting wave cancellation via localised heating elements in boundary layers. *J. Fluid Mech.* **909**, A16.
CHUVAKHOV, P.V. & FEDOROV, A.V. 2016 Spontaneous radiation of sound by instability of a highly cooled hypersonic boundary layer. *J. Fluid Mech.* **805**, 188–206.
CORKE, T.C. & MANGANO, R.A. 1989 Resonant growth of three-dimensional modes in transitioning Blasius boundary layers. *J. Fluid Mech.* **209**, 93–150.
DOVGAL, A.V., LEVCHENKO, V.Y. & TIMOPEEV, V.A. 1990 Boundary layer control by a local heating of the wall. In *Laminar-Turbulent Transition* (ed. D. Arnal & R. Michel), pp. 113–121. Springer.
DOWNS, R.S. & FRANSSON, J.H.M. 2014 Tollmien–schlichting wave growth over spanwise-periodic surface patterns. *J. Fluid Mech.* **754**, 39–74.
FEDOROV, A., SOUDAKOV, V., EGOROV, I., SIDORENKO, A., GROMYKO, Y., BOUNTIN, D., POLIVANOV, P. & MASLOV, A. 2015 High-speed boundary-layer stability on a cone with localized wall heating or cooling. *AIAA J.* **53** (9), 1–13.
KÁTAI, C.B. & WU, X. 2020 Effects of streamwise-elongated and spanwise-periodic surface roughness elements on boundary-layer instability. *J. Fluid Mech.* **899**, A34.
KOROTEEV, M.V. & LIPATOV, I.I. 2009 Supersonic boundary layer in regions with small temperature perturbations on the wall. *SIAM. J. Appl. Math.* **70** (4), 1139–1156.
KOROTEEV, M.V. & LIPATOV, I.I. 2012 Local temperature perturbations of the boundary layer in the regime of free viscous–inviscid interaction. *J. Fluid Mech.* **707**, 595–605.
KRAL, L.D. & FASEL, H.F. 1991 Numerical investigation of three-dimensional active control of boundary-layer transition. *AIAA J.* **29** (9), 1407–1417.
KRAL, L.D., WLEZIEN, R.W., SMITH, J.M. & MASAD, J.A. 1994 Boundary-layer transition control by localized heating: DNS and experiment. In *Transition, Turbulence and Combustion*, pp. 355–367. Springer.
LIEPMANN, H.W., BROWN, G.L. & NOSENCHUCK, D.M. 1982 Control of laminar-instability waves using a new technique. *J. Fluid Mech.* **118**, 187–200.
LIEPMANN, H.W. & NOSENCHUCK, D.M. 1982 Active control of laminar-turbulent transition. *J. Fluid Mech.* **118**, 201–204.
LIN, C.C. 1946 On the stability of two-dimensional parallel flows. III. Stability in a viscous fluid. *Q. Appl. Math.* **3** (4), 277–301.
LIPATOV, I.I. 2006 Disturbed boundary layer flow with local time-dependent surface heating. *Fluid Dyn.* **41** (5), 725–735.
LYSENKO, V.I. & MASLOV, A.A. 1984 The effect of cooling on supersonic boundary-layer stability. *J. Fluid Mech.* **147**, 39–52.
MACK, L.M. 1975 Linear stability theory and the problem of supersonic boundary-layer transition. *AIAA J.* **13** (3), 278–289.
MACK, L.M. 1984 Boundary-layer linear stability theory. AGARD Report 709.
MASAD, J.A. 1995 Transition in flow over heat-transfer strips. *Phys. Fluids* **7** (9), 2163–2174.
MASAD, J.A. & NAYFEH, A.H. 1992 Laminar flow control of subsonic boundary layers by suction and heat-transfer strips. *Phys. Fluids* **4** (6), 1259–1272.
MÉNDEZ, F., TREVIÑO, C. & LIÑÁN, A. 1992 Boundary layer separation by a step in surface temperature. *Int. J. Heat Mass Transf.* **35** (10), 2725–2738.
MULLER, D.E. 1956 A method for solving algebraic equations using an automatic computer. *Mathematical tables and other aids to computation* **10** (56), 208–215.
NEILAND, V.Y. 1969 Theory of laminar boundary layer separation in supersonic flow. *Fluid Dyn.* **4** (4), 33–35.
RENARDY, M. & ROGERS, R.C. 2006 *An Introduction to Partial Differential Equations*, vol. 13. Springer Science & Business Media.
SMITH, F.T. 1979*a* Instability of flow through pipes of general cross-section, part 1. *Mathematika* **26** (2), 187–210.
SMITH, F.T. 1979*b* On the non-parallel flow stability of the Blasius boundary layer. *Proc. R. Soc. Lond.* **366** (1724), 91–109.
SMITH, F.T. 1989 On the first-mode instability in subsonic, supersonic or hypersonic boundary layers. *J. Fluid Mech.* **198**, 127–153.
STEWARTSON, K. & WILLIAMS, P.G. 1969 Self-induced separation. *Proc. R. Soc. Lond.* **312** (1509), 181–206.
THEOFILIS, V. 2011 Global linear instability. *Annu. Rev. Fluid Mech.* **43**, 319–352.
TREVIÑO, C. & LIÑÁN, A. 1996 The effects of displacement induced by thermal perturbations on the structure and stability of boundary-layer flows. *Theor. Comput. Fluid Dyn.* **8** (1), 57–72.
VAN DYKE, M. 1975 *Perturbation Methods in Fluid Mechanics*. The Parabolic Press.

WALTON, A.G. & PATEL, R.A. 1998 On the neutral stability of spanwise-periodic boundary-layer and triple-deck flows. *Q. J. Mech. Appl. Math.* **51** (2), 311–328.

WU, X. & DONG, M. 2016 A local scattering theory for the effects of isolated roughness on boundary-layer instability and transition: transmission coefficient as an eigenvalue. *J. Fluid Mech.* **794**, 68–108.

WU, X. & HOGG, L.W. 2006 Acoustic radiation of Tollmien–Schlichting waves as they undergo rapid distortion. *J. Fluid Mech.* **550**, 307–347.